



Geology and ore genesis of the carbonatite-associated Yangibana REE district, Gascoyne Province, Western Australia

Paul Slezak^{1,2} · Carl Spandler^{1,3} · Andy Border⁴ · Kieren Whittock^{4,5}

Received: 1 November 2019 / Accepted: 28 October 2020 / Published online: 10 November 2020
© Springer-Verlag GmbH Germany, part of Springer Nature 2020

Abstract

The Yangibana rare earth element (REE) district consists of multiple mineral deposits/prospects hosted within the Mesoproterozoic Gifford Creek Carbonatite Complex (GCCC), Western Australia, which comprises a range of rock types including calcite carbonatite, dolomite carbonatite, ankerite–siderite carbonatite, magnetite–biotite dykes, silica-rich alkaline veins, fenite, glimmerites and what have historically been called “ironstones”. The dykes/sills were emplaced during a period of extension and/or transtension, likely utilising existing structures. The Yangibana REE deposits/prospects are located along many of these structures, particularly along the prominent Bald Hill Lineament. The primary ore mineral at Yangibana is monazite, which is contained within ankerite–siderite carbonatite, magnetite–biotite dykes and ironstone units. The ironstones comprise boxwork-textured Fe oxides/hydroxides, quartz, chalcedony and minor monazite and subordinate rhabdophane. Carbonate mineral-shaped cavities in ironstone, fenite and glimmerite alteration mantling the ironstone units, and ankerite–siderite carbonatite dykes altering to ironstone-like assemblages in drill core indicate that the ironstones are derived from ankerite–siderite carbonatite. This premise is further supported by similar bulk–rock Nd isotope composition of ironstone and other alkaline igneous rocks of the GCCC. Mass balance evaluation shows that the ironstones can be derived from the ankerite–siderite carbonatites via significant mass removal, which has resulted in passive REE concentration by ~2 to ~10 times. This mass removal and ore tenor upgrade is attributed to extensive carbonate breakdown and weathering of ankerite–siderite carbonatite by near-surface meteoric water. Monazite from the ironstones has strong positive and negative correlations between Pr and Nd, and Nd and La, respectively. These relationships are reflected in the bulk–rock drill assays, which display substantial variation in the La/Nd throughout the GCCC. The changes in La/Nd are attributed to variations in primary magmatic composition, shifts in the magmatic-hydrothermal systems related to CO₂ versus water-dominated fluid phases, and changes in temperature.

Keywords Rare earth element · Monazite · Gifford Creek Carbonatite Complex · Radiogenic isotopes · Carbonatite · Weathering

Editorial handling: R. Linnen

Supplementary Information The online version contains supplementary material available at <https://doi.org/10.1007/s00126-020-01026-z>.

✉ Paul Slezak
paul.slezak@ucd.ie

¹ Geoscience, College of Science and Engineering, James Cook University, Townsville, QLD 4811, Australia

² School of Earth Sciences, University College Dublin, Dublin D04 N2E5, Ireland

³ Department of Earth Sciences, The University of Adelaide, Adelaide, SA 5005, Australia

⁴ Hastings Technology Metals Ltd., Level 8 Westralia Plaza, 167 St. Georges Terrace, Perth, WA 6000, Australia

⁵ Whittock Geological Pty Ltd., 7/3-5 Riverside Crescent, Marrickville, NSW 2204, Australia

Introduction

Carbonatites are peralkaline-alkaline igneous rocks containing $\geq 50\%$ primary carbonate minerals (Le Maitre 2002) and are the most important primary source for critical metals such as rare earth elements (REE) and high field strength elements (HFSE) (Chakhmouradian and Zaitsev 2012; Wall 2014; Goodenough et al. 2016). Although REE deposits associated with peralkaline-alkaline silicate igneous rocks typically contain higher tonnages, they often have lower grades and poorer REE recovery than carbonatite-hosted REE deposits (Walters et al. 2011; Wall 2014). Not surprisingly, the largest currently-producing mines for REE (Bayan Obo, China; Maoniuping, China; and Mount Weld, Australia) and Nb (Araxá, Brazil; Catalão I and II, Brazil; and St-Honoré, Canada) are all carbonatite-associated critical metal deposits (Mitchell 2015; Elliott et al. 2018). In many cases, the economic viability of mining carbonatite deposits relies on natural post-magmatic enrichment processes (Verplanck et al. 2016). Niobium enrichment often happens through eluvial supergene processes (Morteani and Preinfalk 1996; Mitchell 2015). Rare earth element enrichment occurs when REE (fluor)carbonates are dissolved and re-precipitated as minerals such as monazite or gorceixite under low temperature, supergene conditions (Morteani and Preinfalk 1996).

Australia hosts a variety of different REE deposits, including several carbonatite deposits such as Mount Weld, Cummins Range and the Yangibana REE district (Jaireth et al. 2014). The Yangibana REE district has a currently defined total mineral resource of 21.3 million tonnes of ore grading 1.12% TREO, all hosted by the Gifford Creek Carbonatite Complex (GCCC). These deposits are particularly rich in Pr and Nd that are hosted mainly in monazite within ironstone dykes (Hastings Technology Metals 2019). The ironstone dykes or “ironstones”, as they have historically been called, are not Fe-rich sedimentary rocks as their name might imply; they occur as anastomosing dykes and sills that cross-cut the Paleo- to Mesoproterozoic granitic, metasedimentary and sedimentary rocks in the area. Previous works have focused on the Lyons River Sills, which are calcite and dolomite carbonatite dykes and sills that comprise most of the GCCC (Pearson 1996; Pearson and Taylor 1996; Pearson et al. 1996; Pirajno et al. 2014). However, recent work has also identified unaltered ankerite–siderite carbonatite and magnetite–biotite dykes as important components of the GCCC (Slezak et al. 2018; Slezak and Spandler 2019, 2020). These newly recognised rock types are significant because they host considerable monazite mineralisation and their Fe-rich bulk composition makes them feasible protoliths to the REE-enriched ironstones.

While recent work has progressed understanding of the petrological (Pirajno et al. 2014; Slezak and Spandler 2020) and temporal (Zi et al. 2017; Slezak and Spandler 2019)

evolution of the GCCC, there has been little research into processes of ore formation and REE distribution within the Yangibana REE district. This is particularly noteworthy, as mineralisation at Yangibana occurs as monazite-rich dyke sets instead of the common association with REE carbonate plugs and ring structures of most mineralised carbonatite complexes (Barker 1989). In this study, we examine the geological setting, distribution and origins of the REE ores within the Yangibana REE district using a combination of field mapping, bulk–rock geochemistry and REE phosphate chemistry. Integrating our new data with previous information on the GCCC, we outline the causes for Nd variation in ore monazite throughout the district and present a new ore genesis model for the district. This in turn can assist in developing better methods for mineral exploration and processing, both at Yangibana and in carbonatite complexes more broadly.

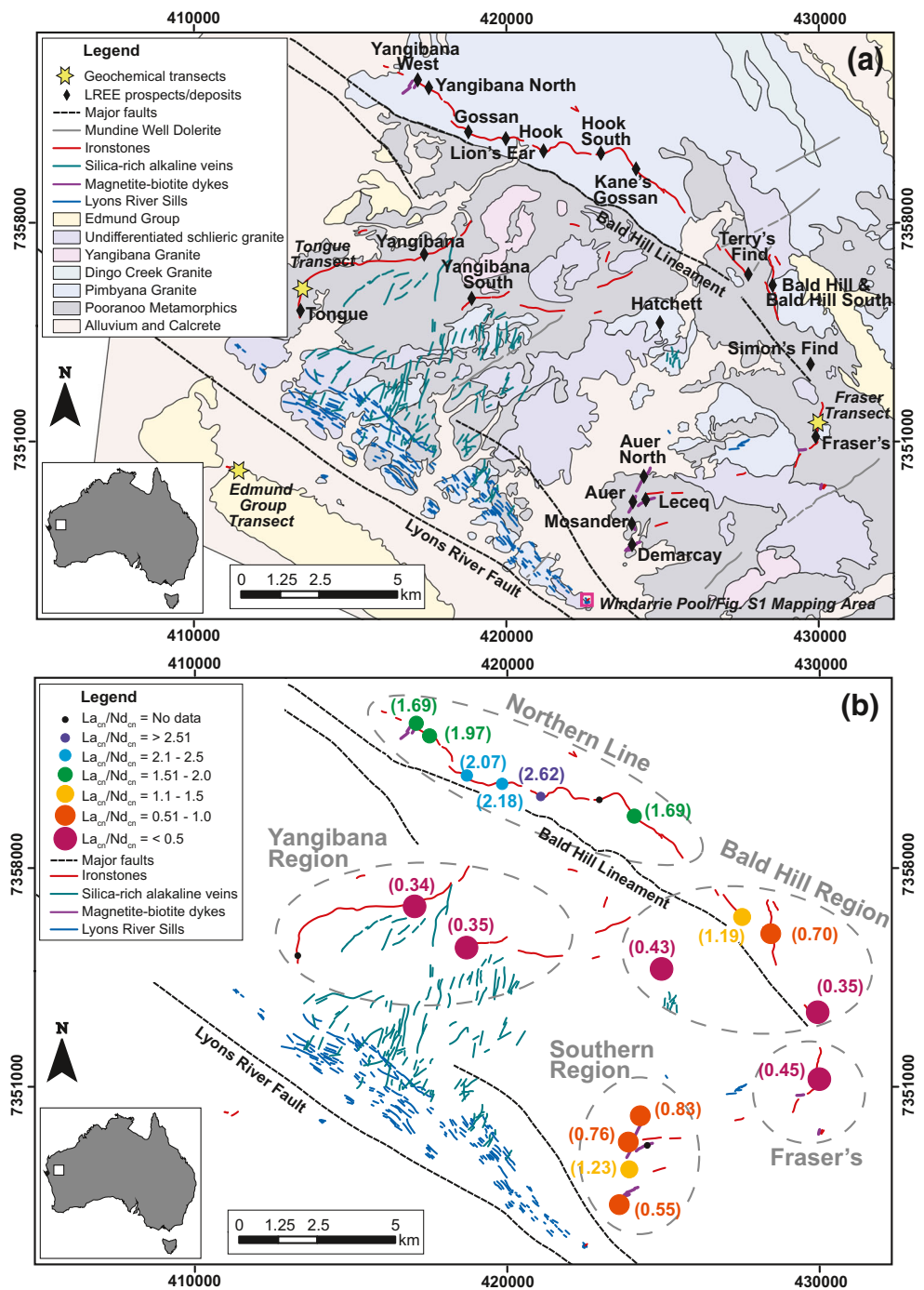
Regional geology

The Yangibana REE district is hosted by the GCCC in the Gascoyne Province of Western Australia. The Gascoyne Province comprises mainly Paleo- to Mesoproterozoic granitic rocks, gneisses and other metasedimentary rocks that have undergone over 1 b.y. of terrane assembly and reworking related to at least eight significant orogenic events (Sheppard et al. 2010; Johnson et al. 2013, 2017; Cutten and Johnson 2018).

The GCCC presents as a series of dykes and sills that primarily intrude the Mesoproterozoic Durlacher Supersuite granitoids (locally including Pimbyana and Yangibana granites) and the Pooranoo Metamorphics in the region between the Lyons River Fault and the Bald Hill Lineament (Fig. 1). However, some small dykes are present south of the Lyons River Fault in the Edmund Group metasedimentary rocks, and some alkaline dykes and sills have been found immediately to the north of the Bald Hill Lineament (Fig. 1). The GCCC sits adjacent to the Lyons River Fault, which has been determined via seismic reflection surveys to extend down to, and offset, the Mohorovičić Discontinuity (Johnson et al. 2013). The Lyons River Fault is a major shear zone that sutured the Neoproterozoic Glenburgh Terrane with the Archean Pilbara Craton during the 2215 to 2145 Ma Ophthalmia Orogeny (Sheppard et al. 2005; Johnson et al. 2011, 2013). It was later reactivated as an extensional structure prior to, and after the 1680 to 1620 Ma Mangaroon Orogeny (Sheppard et al. 2005), and again as a reverse fault system during the 1320 to 1170 Ma Mutherbukin Tectonic Event (Korhonen et al. 2015; Johnson et al. 2013).

After emplacement of the GCCC at 1370 Ma (Zi et al. 2017; Slezak and Spandler 2019), the region was subjected to several major tectonomagmatic events, including the 1320 to 1170 Ma Mutherbukin Tectonic Event (Korhonen et al.

Fig. 1 a Geologic map of the Gifford Creek Carbonatite Complex (GCCC) with deposit/prospect locations and sampling transect locations. Figure S1 is located in ESM 1. **b** Distribution of La_{cn}/Nd_{cn} values based on Hasting Technology Metals drill assay data. Five major deposit/prospect regions are circled. The lowest La_{cn}/Nd_{cn} values (highest Nd concentrations) are located in the central and east central regions of the GCCC (modified after Slezak et al. 2018)

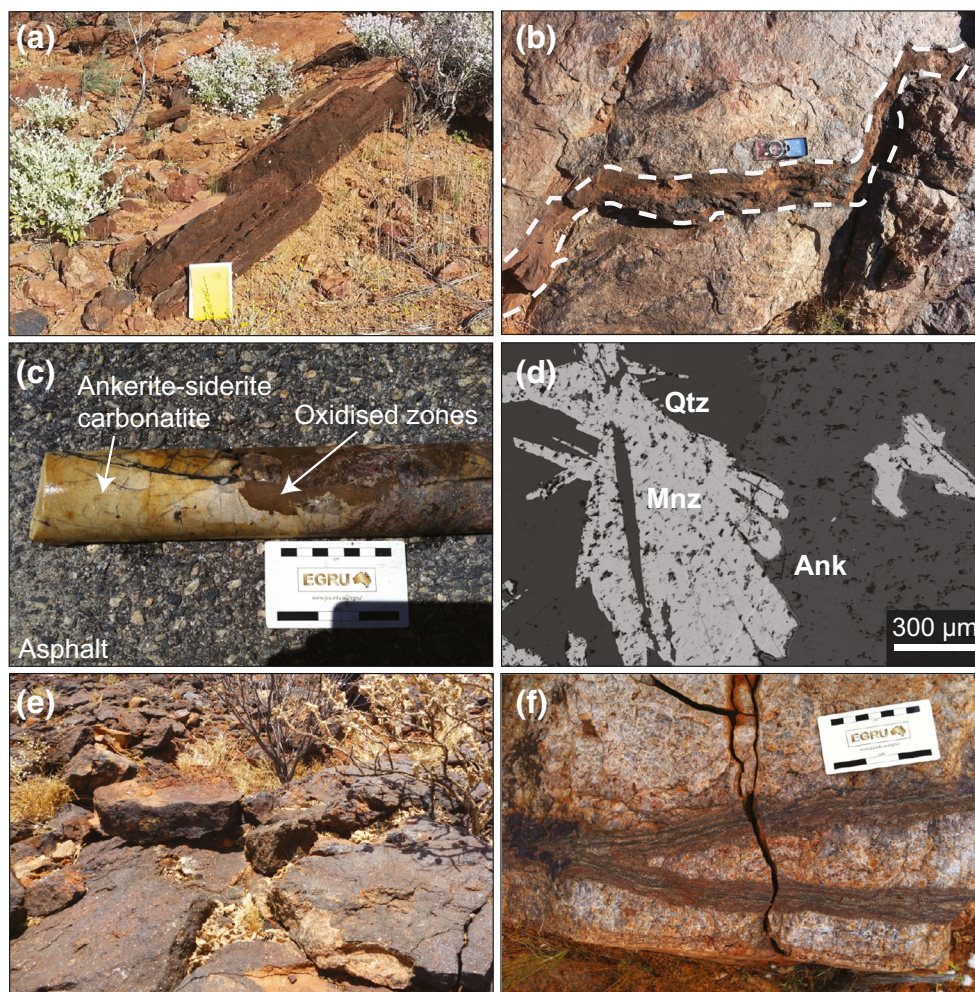


2015), the 1090 to 1040 Ma Giles Event (Smithies et al. 2015), the 1030 to 950 Ma Edmundian Orogeny (Martin and Thorne 2004; Sheppard et al. 2007), the 955 to 830 Ma Kuparr Tectonic Event (Cutten and Johnson 2018; Olierook et al. 2019) and the 570 Ma Mulka Tectonic Event (Sheppard et al. 2010). Some of these events are recorded by U–Pb ages and Sm–Nd isochron ages from GCCC monazite and apatite that have undergone dissolution and precipitation (Pirajno et al. 2014; Zi et al. 2017; Slezak and Spandler 2019).

Geology of the Gifford Creek Carbonatite Complex

The GCCC comprises multiple rock types, which are described briefly below. More detailed rock-type descriptions are presented in Slezak and Spandler (2020). The primary magmatic-hydrothermal units include dolomite and calcite carbonatite that form the Lyons River Sills, ankerite–siderite carbonatite, magnetite–biotite dykes and silica-rich alkaline

Fig. 2 Field photos and backscattered electron (BSE) images of GCCC rock types. **a** Lyons River Sill dolomite carbonatite with typical dark brown weathering surface and dipping southwest towards the Lyons River Fault. **b** Lyons River Sills with a “z”-shaped step-over and deflection of the dyke by a pegmatitic section of schlieric granite. **c** Core samples of ankerite–siderite carbonatite from Yangibana North with patchy alteration to iron oxides, similar to the ironstones. **d** BSE image of monazite growing in both the quartz and ankerite domains of the ankerite–siderite carbonatites with a narrow Fe oxide rim surrounding the monazite in the ankerite. **e** Coarse-grained magnetite–biotite dyke at Mosander with a nearly flat-lying, sill morphology. **f** Silica-rich alkaline vein from the central GCCC with arfvedsonite-riebeckite (dark) and aegirine (light) layers



veins. Alteration phases associated with these primary rock types include the Yangibana ironstones, fenites and glimmerites.

Lyons River Sills

The Lyons River Sills (Fig. 2a, b) mainly occur as a swarm of carbonatite dykes/sills trending NW–SE immediately to the north of the Lyons River Fault. The Lyons River Sills are composed of fine-grained, Fe-bearing dolomite and occasionally calcite, minor amounts of Mg- and F-rich arfvedsonite, aegirine, Mg-bearing biotite, magnetite, ilmenite and fluorapatite in addition to trace amounts of monazite, zircon, pyrite and chalcopyrite (Pearson 1996; Pearson and Taylor 1996; Pearson et al. 1996; Slezak and Spandler 2020).

The Lyons River Sills strike northwest and dip variably 30 to 60° SW (Electronic Supplementary Material (ESM 1); Fig. S1a), subparallel with the Lyons River Fault and Bald Hill Lineament (Fig. 1). They are 0.1 to 1.5 m thick and may extend hundreds of metres in length. Mapping of well-exposed outcrops close to the Lyons River towards the

southern extent of the dyke/sill swarm (Fig. 1 and ESM 1, Fig. S1) reveals that metre-scale orientations and morphologies of veins (~1–9 cm thick), veinlets (~1–9 mm thick) and joints (ESM 1, Fig. S1) are analogous to district-scale dyke and fault orientations (Fig. 1). For example, outcrop scale alkaline amphibole–dolomite veins and veinlets (3 to 20 mm wide), which are akin to the ironstones, are observed to trend orthogonal to the Lyons River Fault (ESM 1, Fig. S1b, c), whereas the carbonatite dykes are oriented along joint sets that parallel the Lyons River Fault (ESM 1, Fig. S1c). The silica-rich alkaline veins (Fig. 1) also broadly correspond to the N–S joint sets recorded at the outcrop scale (ESM 1, Fig. S1b). Step-over patterns and veinlet pinch outs are also common among the Lyons River Sills at both district and outcrop scales (Figs. 1 and 2b and ESM 1, Fig. S1d).

Ankerite–siderite carbonatite

The ankerite–siderite carbonatite (Fig. 2c) has only been observed in drill core at depths of 40 to 50 m in the northwestern corner of the GCCC along the Bald Hill Lineament. These

rocks occur as 0.05 to 1 m thick dykes (Fig. 2c) composed of coarse-grained siderite and ankerite, with minor calcite, magnetite, biotite, monazite, apatite and quartz (Fig. 2d; Slezak et al. 2018; Slezak and Spandler 2020).

Magnetite–biotite dykes

Magnetite–biotite dykes (Fig. 2e) are present mainly in the southeast region between Fraser's deposit and Demarcay prospect (Fig. 1). They range in thickness from 0.1 to 1.5 m and comprise magnetite, biotite, apatite and monazite (Slezak and Spandler 2020). Several magnetite–biotite dykes, such as the Auer North prospect, do not crop out, but were discovered during exploration drilling. The units that appear at the surface, such as at Demarcay and Mosander, dip variably to the west-northwest.

Silica-rich alkaline veins

The silica-rich alkaline veins (Fig. 2f) are most abundant as steeply dipping, N- to NE-trending swarm in the central region of the GCCC. Some veins display alternating changes in light green aegirine and dark blue arfvedsonite content (Fig. 2f). Individual veins can be up to 50 cm in width, several hundred metres in length, and tend to be heterogeneous in mineralogy and texture. The dominant mineralogy is aegirine, quartz, zircon, rutile, magnetite, phlogopite, columbite and monazite (Slezak and Spandler 2020). These units strike north–northeast, roughly orthogonal to the Lyons River Sills (Fig. 1) and tend to follow regional cleavage fabrics and joint planes (ESM 1, Fig. S1c).

Ironstone dykes

Other rock types present in the GCCC include the voluminous and economically important ironstones and various alteration assemblages such as fenites and glimmerites. The ironstones specifically refer to large (up to several metres wide) dyke-like structures that protrude from the landscape (Fig. 3a). They are mainly located subparallel to the Bald Hill Lineament and along the eastern and western flanks of the GCCC (Fig. 1).

The ironstones comprise fine-grained haematite with relict magnetite cores, recrystallised quartz, occasional baryte, monazite, apatite, rhabdophane and Mn oxides. The ironstones do not exhibit any primary igneous textures. Most features relate to low-temperature mineral precipitation and include botryoidal banding of Mn oxides and hydrous Fe oxides, such as goethite. Minor chalcedony banding around open spaces and Mn oxide crusts have also been reported (Pirajno and González-Álvarez 2013). The ironstones observed from surface outcrops and from drill core contain significant vugs. In addition, carbonate mineral dissolution cavities (Fig. 3b, c)

and Fe oxides/hydroxides pseudomorphing carbonate minerals were observed at several ironstone outcrops.

In drill core, the ankerite–siderite carbonatite is partially altered and oxidised to a porous, haematite-rich rock similar to the ironstones observed at the surface (Figs. 2c and 3c, d). Some of the oxidised zones occur proximal to veinlets containing magnetite (altering to haematite) and biotite (Fig. 3c). Monazite occurs in large (up to 400 µm) tabular crystals surrounded by dog-tooth-shaped carbonate crystals (likely calcite) hosted in iron oxides such as haematite and goethite (Fig. 3e).

Small veinlets, reminiscent of the larger ironstones, are also observed to emanate from the Lyons River Sills (Fig. 3f). These veinlets have a northeast-southwest strike and dip subvertically to vertically. They are often composed of Fe oxide minerals, but occasionally exhibit a primary mineral assemblage of arfvedsonite, Fe-bearing dolomite, rutile, magnetite, quartz, apatite and monazite; hence, where unaltered, they are referred to as alkaline amphibole–dolomite veinlets in this study.

Alteration assemblages

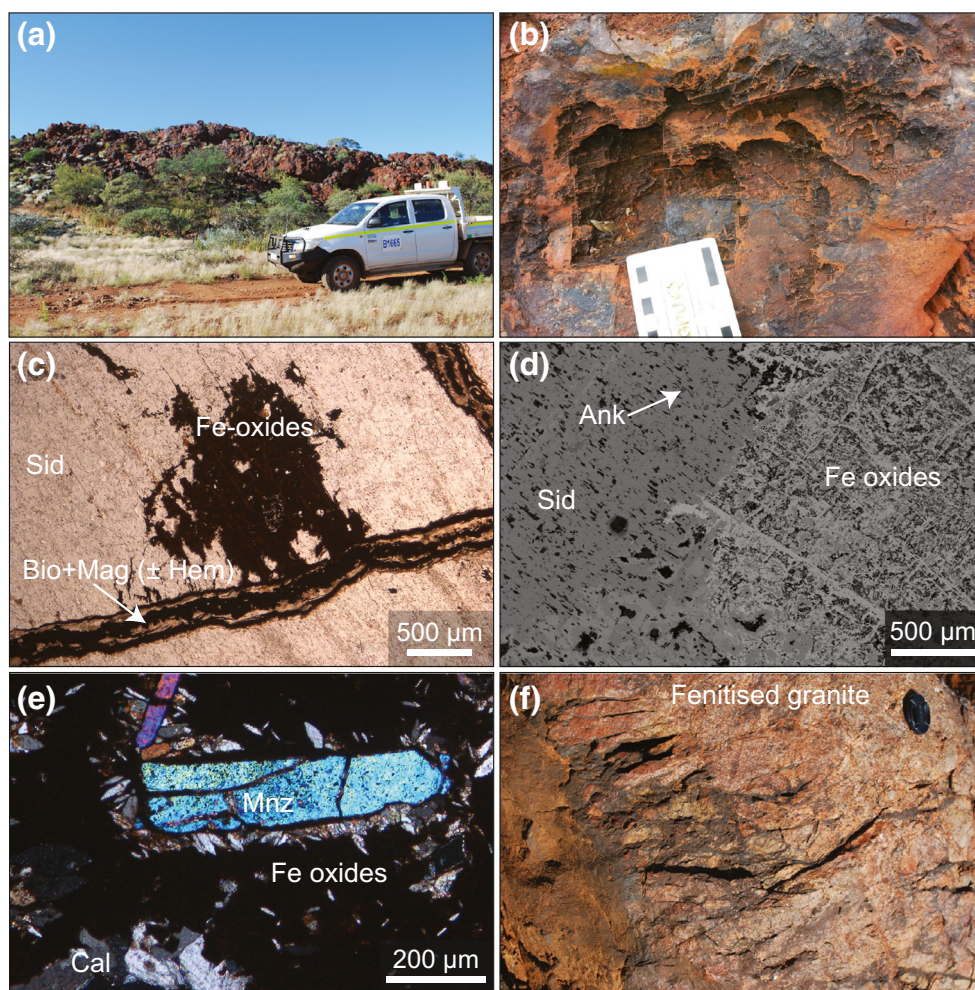
The two most common alteration assemblages in the GCCC are fenite and glimmerite. The fenite assemblage is pink (Fig. 3f) to white and mainly comprises K-feldspar with lesser amounts of apatite, monazite and rare microcrystalline quartz (Slezak and Spandler 2020). The alteration is pervasive and envelopes all the alkaline rock phases in the complex, but is most conspicuous around the ironstones, ankerite–siderite carbonatites and the Lyons River Sills. It is a few centimetres wide around veins and veinlets, and up to a couple of metres wide around larger dykes (Slezak et al. 2018).

Glimmerite is composed of biotite, magnetite, monazite and zircon and forms narrow, contact alteration halos between the fenitised wall-rock and the ankerite–siderite carbonatite dykes. The assemblage may also occur as a series of small veinlets in crackle breccia in the host rocks (Slezak and Spandler 2020).

Yangibana REE deposits and prospects

Multiple mineral deposits and prospects comprise the Yangibana REE district. The district is divided into five areas based on regional structural features, La/Nd ratio, the host rock types and the associated unaltered protolith rock types (Fig. 1). The Yangibana region comprises the Yangibana, Yangibana South and Tongue prospects, all of which crop out as large, east–northeast striking ironstones hosted in the metasedimentary rocks of the Pooranoo Metamorphics. The geometry of these prospects is controlled by the Mangaroon Orogen S_1 compositional layering and F_1 folding within the host rocks, which are later overprinted by a S_2 crenulation

Fig. 3 Field and photomicrographs of ironstones and alteration assemblages. **a** Ironstone outcrop at Fraser's deposit. **b** Ironstone with parallelepiped-shaped dissolution cavities morphologically similar to crystalline carbonate minerals. **c** Dissolution and oxidation in an ankerite–siderite carbonatite adjacent to a magnetite–biotite veinlet. **d** BSE image of the contact between unaltered ankerite–siderite and a zone altered to iron oxides. **e** Monazite rimmed by calcite in the oxidised (i.e. haematite-rich), ironstone-like zones of altered ankerite–siderite carbonatite. **f** Alkaline amphibole–dolomite veinlets emanating from a dolomite carbonatite dyke (Lyons River Sill). The veins (left side of image) have intruded and fenitised the host granite



cleavage (Sheppard et al. 2005). The prospects contain very low La_{cn}/Nd_{cn} values (< 0.5 ; Fig. 1b; where $_{cn}$ = condrite-normalised), and the unaltered protolith of the ironstones has not presently been observed in outcrop or drill core.

The Northern Line comprises seven prospects that present along a nearly continuous, anastomosing ironstone outcrop that runs sub-parallel to the Bald Hill Lineament. The ironstone dykes intrude the Pimbyana and Yangibana granites. Mineralisation contains higher La_{cn}/Nd_{cn} values (> 1.51 ; Fig. 1b) and occurs where the ironstone outcrops are the most prominent at surface, dipping variably to the south–southwest. Ankerite–siderite carbonatite and magnetite–biotite dykes have been encountered at depth in drill core in the Yangibana West and Yangibana North deposits (Fig. 2c).

The Bald Hill region consists of the Bald Hill and Bald Hill South, Terry's Find, Simon's Find and Hatchet prospects. The largest deposits, Bald Hill and Bald Hill South, each consist of a shallowly dipping (15 to 30° SW) ironstone unit hosted in schlieric Pimbyana Granite near the surface and pelitic metasedimentary rocks (likely the Pooranoo Metamorphics) at depth. The mineralised zones have low to moderate La_{cn}/Nd_{cn} values (0.35–1.19; Fig. 1b) and are contained mainly in the ironstones and in subordinate magnetite–biotite rock assemblages.

The easternmost deposit, Fraser's, consists of one large (Fig. 3a), steeply dipping (55 to 65°W) ironstone that intrudes along a contact between Pimbyana Granite and schists of the Pooranoo Metamorphics. The deposit contains altered ankerite–siderite carbonatite at depth (~ 100 m below surface) and is spatially associated with several small magnetite–biotite and carbonatite dykes. Fraser's deposit has a low La_{cn}/Nd_{cn} value of < 0.5 (Fig. 1b).

The Southern Region consists of the Auer, Auer North, Leceq, Mosander and Demarcay prospects, which strike NW–SE and are hosted mainly in schists of the Pooranoo Metamorphics. These prospects comprise both ironstones and magnetite–biotite dykes and contain moderate La_{cn}/Nd_{cn} values (0.55–1.23; Fig. 1b).

Analytical techniques

Samples

This study analysed 28 samples collected from outcrop, 7 samples taken from diamond drill core and 2 samples acquired

from reverse circulation drill cuttings. Details of the sample type, location and analytical techniques can be found in Electronic Supplementary Materials (ESM 2). Sixteen samples were analysed for bulk–rock chemical composition (ESM 2, Table S1) and 5 samples for bulk–rock Nd isotopes (Table 1). Nineteen samples for were used for wavelength dispersive X-ray spectroscopy (WDS) analyses (ESM 2, Table S2), and 9 samples were used for laser ablation inductively coupled mass spectrometry (LA-ICP-MS) analysis (ESM 2, Table S3).

Cathodoluminescence and major element analyses of ore minerals

All REE ore samples were prepared as polished thin sections and 25-mm-diameter polished sections, which were examined using a Leica DMRXP optical microscope. Cathodoluminescence (CL) analyses of the main ore mineral, monazite, were conducted using a JEOL XM-86440 CL spectrometer connected to the JEOL JXA-8200 WD/ED electron probe micro-analyser (EPMA) at the Advanced Analytical Centre at James Cook University (JCU), Townsville, Australia, using the same setup and conditions as those in Slezak et al. (2018). Deconvolution of these spectra was conducted using the Optical Fit 17.07 software from CSIRO (Torpy and Wilson 2008).

After CL analysis, the samples were analysed for major/minor elements in monazite and rhabdophane using the JEOL JXA-8200 EPMA at JCU. The electron beam was set to spot size of 2 to 5 μm, with the accelerating voltage and beam current set to 15 kV and 20 nA, respectively. All elements were analysed for 20s on peak with 10s on background. Element concentrations were quantified using well-characterised, in-house standards as follows: Ca and Si (wollastonite), Sr (SrF₂), P and Ce (CePO₄), Nd (NdPO₄), Sm (SmPO₄), Pr (PrPO₄), Y (YPO₄), Gd (GdPO₄), Dy (DyPO₄), La (LaPO₄) and Th (Th metal). The φρz procedure was used to correct the analyses (Armstrong 1991).

Trace element analysis of monazite

Trace elements analyses of monazite were analysed using a Coherent GeoLasPro 193-nm Excimer laser coupled to a Varian (now Bruker) 820-MS quadrupole ICP-MS at the Advanced Analytical Centre, JCU Townsville. The glasses were ablated in a large volume cell (Fricker et al. 2011), using a 24-μm-spot size, repetition rate of 10 Hz, and surface energy density (measured at the site of ablation) of 4 J/cm². The ablated material was carried in high purity He gas then mixed with Ar before being introduced to the ICP-MS. The rates of oxide production and plasma fractionation were monitored by keeping ThO/Th at or below 0.5%, and ²³⁸U/²³²Th sensitivity ≈ 1 (Pettker 2008). The synthetic glasses NIST SRM 610 and 612 were used as the primary and secondary standards, respectively,

Table 1 Bulk–rock Sm–Nd isotope results for outcrop samples of ironstones, fenites and the Pimbyana Granite

Sample	LE-1	YN-1	FT-1	FT-3	FT-7
Easting	420,072	417,377	429,894	429,913	429,926
Northing	7,360,691	7,362,372	7,350,903	7,350,912	7,350,811
Rock type	Ironstone	Ironstone	Ironstone	Fenitised Pimbyana Granite	Pimbyana Granite
Rock age, t (Ma)	1370	1370	1370	1370/1680*	1370/1680*
Nd, μg/g	4140	1520	1020	82.4	34.8
Sm, μg/g	531	161	98.7	14.8	5.76
¹⁴⁷ Sm/ ¹⁴⁴ Nd	0.0776	0.0641	0.0586	0.109	0.100
¹⁴³ Nd/ ¹⁴⁴ Nd	0.511474	0.511280	0.511316	0.511730	0.511261
¹⁴⁵ Nd/ ¹⁴⁴ Nd(t)	0.510775	0.510703	0.510789	0.510753/0.5105307*	0.510361/0.510156*
εNd(t)	−1.83	−3.24	−1.55	−2.26/1.27*	−9.93/−6.07*
T _{DM} (Ma)	1860	1890	1790	2040	2500
T _{CHUR} (Ma)	1490	1560	1460	1570	2160

*1680 Ma date is from Pearson et al. (1996) and is granite crystallisation age

with reference values taken from Spandler et al. (2011). The Ce contents, as determined by EPMA WDS, were used as internal standards for monazite. Data reduction was carried out using the SILLS program (Guillong et al. 2008), employing the errors and detection limits calculation methods of Luo et al. (2007) and Pettke et al. (2012), respectively. The isotopes chosen for analysis include: ^{27}Al , ^{29}Si , ^{31}P , ^{43}Ca , ^{44}Ca , ^{49}Ti , ^{55}Mn , ^{66}Zn , ^{75}As , ^{85}Rb , ^{88}Sr , ^{89}Y , ^{90}Zr , ^{93}Nb , ^{118}Sn , ^{133}Cs , ^{137}Ba , ^{139}La , ^{140}Ce , ^{141}Pr , ^{143}Nd , ^{147}Sm , ^{151}Eu , ^{157}Gd , ^{159}Tb , ^{163}Dy , ^{165}Ho , ^{167}Er , ^{169}Tm , ^{171}Yb , ^{175}Lu , ^{178}Hf , ^{181}Ta , ^{208}Pb , ^{232}Th and ^{238}U .

Bulk-rock trace element data

Bulk-rock transect samples

Sampling transects were completed across the ironstone dykes at Fraser's deposit and Tongue prospect, which cross-cut the Pimbyana Granite and Pooranoo Metamorphics, respectively (Fig. 1a). A third sample transect was taken across a subeconomic ironstone dyke intruding the Edmund Group to the southwest of the Lyons River Fault (Fig. 1a). Samples were taken directly from the ironstone, which was considered to be the start (0 m) of the transect. Additional samples were taken at available outcrops including the contact between the ironstone and the fenite, within the fenite (centimetres to metres from the transect start), and in the least-altered host rock (metres to tens of metres from the transect start). Any visible surficial weathering rinds were trimmed and discarded. The purpose was to identify the extent of alteration related to the ironstone intrusions and to assess geochemical exchange between the host rocks and ironstone or their precursor igneous intrusion. The location, sample type and geochemical summary are found in *ESM 2*, Table S1.

All samples were crushed and then milled to a fine powder using a tungsten carbide ring mill. Fraser's transect samples were analysed for major element composition from Li borate fusion glasses at JCU, using a Bruker-AXS S4 Pioneer X-ray Fluorescence Spectrometer. The fused glasses were then mounted into 25-mm-diameter epoxy sections and were analysed using the LA-ICP-MS instrument and analytical conditions as previously mentioned for the monazite samples, except in this case a spot size of 120 μm and surface energy density of 6 J/cm^2 was applied. The following analytes were measured for the glasses: ^9Be , ^{27}Al , ^{29}Si , ^{31}P , ^{43}Ca , ^{44}Ca , ^{45}Sc , ^{49}Ti , ^{52}Cr , ^{53}Cr , ^{55}Mn , ^{57}Fe , ^{59}Co , ^{60}Ni , ^{65}Cu , ^{66}Zn , ^{69}Ga , ^{72}Ge , ^{75}As , ^{85}Rb , ^{88}Sr , ^{98}Mo , ^{121}Sb , ^{89}Y , ^{90}Zr , ^{93}Nb , ^{118}Sn , ^{133}Cs , ^{137}Ba , ^{139}La , ^{140}Ce , ^{141}Pr , ^{143}Nd , ^{147}Sm , ^{151}Eu , ^{157}Gd , ^{159}Tb , ^{163}Dy , ^{165}Ho , ^{167}Er , ^{169}Tm , ^{171}Yb , ^{175}Lu , ^{178}Hf , ^{181}Ta , ^{208}Pb , ^{232}Th and ^{238}U . The data were reduced using Glitter software (Van Acherbergh et al. 2001).

Samples from the Tongue and Edmund Group ironstone transects were analysed for 53 elements by Bureau Veritas Commodities Canada Ltd. in Vancouver, Canada. One sample

split was fused into a lithium metaborate/tetraborate bead. The sample bead was dissolved in American Chemical Society (ACS)-grade nitric acid dissolution and analysis of the solution conducted via ICP-MS for the following elements: Mg, Al, Si, P, K, Ca, Sc, Ti, V, Cr, Mn, Fe, Ni, Ga, Rb, Sr, Y, Zr, Nb, Sn, Cs, Ba, La, Ce, Pr, Nd, Sm, Eu, Gd, Tb, Dy, Ho, Er, Tm, Yb, Lu, Hf, Ta, W, Th and U. The second sample split was digested in aqua regia and analysed via inductively coupled emission spectroscopy/mass spectroscopy (ES/MS) for the elements Li, Be, B, Cr, Co, Cu, Zn, Ge, As, Se, Mo, Pd, Ag, Cd, In, Sb, Te, Re, Pt, Au, Hg, Tl, Pb and Bi. Carbon and S were determined using the LECO method.

Drill hole data

Data from 15,185 bulk-rock assays were provided by Hastings Technology Metals Ltd. for use in determining regional- and deposit-scale REE trends. Approximately 1–2 kg of material was taken from 1-m intervals of reverse circulation (RC) cuttings and diamond drill core. Samples were prepared using a sodium peroxide fusion in a Ni crucible then analysed for Mg, Al, Si, P, S, Ca, Mn and Fe using OE-MS, as well as Sc, Sr, Y, Zr, Nb, Ba, La, Ce, Pr, Nd, Sm, Gd, Tb, Dy, Ho, Er, Tm, Yb, Lu, Ta, Th and U using ICP-MS at Intertek-Genalysis in Perth (Australia). As many of these samples represent rock-type composites, we applied a lower cut-off concentration of 40 wt.% Fe to the Hastings data to define the composition of the ironstones. Applying this filter to the data from the Yangibana North prospect (where most ironstone data exist) resulted in 51 samples, which were used to determine an average ironstone composition for mass balance comparisons. Bulk-rock mass balance calculations were made using bulk-rock geochemical data and following the methods of Gresens (1967) and Grant (1986) using the EASYGRESGRANT Excel macros and spreadsheets (López-Moro 2012).

Bulk-rock Sm–Nd isotope analysis

Whole-rock Sm–Nd isotope analyses of 5 samples from deposit outcrops and transect samples (three ironstones, one fenite and one Pimbyana Granite) were performed at the University of Adelaide with a Finnigan MAT262 thermal ionisation mass spectrometer (TIMS) in static and quadrupole cup dynamic measurement modes following the routine described in Wade et al. (2006). The measurements were corrected for mass fractionation by normalisation to $^{146}\text{Nd}/^{142}\text{Nd} = 0.7219$ and $^{143}\text{Nd}/^{144}\text{Nd}$ ratios were normalised to the TIMS value of JNdi-1 glass (0.512098 ± 13 ; Fisher et al. 2011). Details of the samples are presented in Table 1.

Results

Ore minerals

Monazite is the main ore mineral in the Yangibana REE district and the majority consists of (Ce)–monazite, though some grains transition to (Nd)–monazite (ESM2, Table S2). Monazite is found in highest concentration in the ironstone deposits, magnetite–biotite dykes and ankerite–siderite carbonatite. Trace amounts of monazite are also present in the silica-rich alkaline veins, occurring together with more abundant zircon (Slezak and Spandler 2020). Monazite is only present as trace amounts in the Lyons River Sills, which instead contain greater amounts of apatite.

Monazite makes up between ~1 and ~10% by volume of the magnetite–biotite dykes, ankerite–siderite carbonatite and their alteration assemblages (fenite and glimmerite). The monazite is often cream to peach colour and forms large (~2 mm) clusters of subhedral to euhedral tabular crystals. Less commonly, monazite forms small, anhedral inclusions (~10 µm) in apatite, which may be the product of exsolution (Slezak et al. 2018). In high-contrast backscattered electron (BSE) and CL images, monazite often exhibits patchy, irregular dark and light grey zonation (Fig. 4a) as well as occasional oscillatory growth zones (Fig. 4b). The lighter BSE zones are typically associated with higher Th contents, as determined by EDS. Large monazite grains (up to 1 mm long) hosted in the ironstones also have a tabular morphology, similar to monazite in ankerite–siderite carbonatite and magnetite–biotite dykes. However, these large monazite crystals are often fractured, have irregular margins and are occasionally mantled by a slightly darker (in BSE) REE-bearing mineral phase with an amorphous to acicular crystal habit (Fig. 4c, d). This phase has relatively high CaO contents and is likely rhabdophane [(REE, Ca, Th)PO₄·nH₂O]. It is often found together with botryoidal and boxwork-textured iron oxides and hydroxides like goethite (Fig. 4d).

Monazite mineral chemistry

Under CL, monazite displays patchy zonation in cores and rims (Fig. 4e). Counts are elevated from ~350 nm up to ~600 nm and distinct peaks occur at 784 nm, 857 nm, and 1048 nm (Fig. 4f). Both light and dark CL zones have similar spectral shapes, but the lighter zones show higher counts at the 857 nm peak. The full width at half maximum (FWHM) and eV values for the probable peak locations can be found in ESM 1, Fig. S2 and Table S1.

Monazite has low Si (<1 wt.% SiO₂), low Ca (<1 wt.% CaO) and variable Th (0.5 to 10 wt.% ThO₂; ESM 2, Table S2). Thorium and Ca contents are inversely proportional to the total REY (REE + Y; Fig. 5a). Additionally, Si and Th correlate with a decrease in REY and P content in monazite

(Fig. 5b). No correlations were observed between Th and individual REE or Y. Monazite in the Lyons River Sills and their associated alkaline amphibole–dolomite veinlets contains higher amounts of Ca, Th and Si compared to the monazite from ankerite–siderite carbonatite and magnetite–biotite dykes (Fig. 5a, b).

Lanthanum and Nd show a strong, negative correlation in monazite. The alkaline amphibole–dolomite veinlets and Lyons River Sills have the highest La contents and lowest Nd contents (Fig. 5c). Cerium and Nd show no clear correlation (Fig. 5d). However, Nd shows a strong positive correlation with Pr (Fig. 5d) and a moderate positive correlation with Sm. Monazite from the ironstones and fenites has the highest contents of REE such as Pr, Nd and Sm.

Arsenic and Nd contents have a strong, positive correlation (ESM 1, Fig. S3a), but As and Yb show no correlation (ESM 1, Fig. S3b). Strontium contents reach up to 2 wt.% with Sr content correlating with both Th and Pb contents (ESM 1, Fig. S3c). Monazite in the alkaline amphibole–dolomite veinlets has the highest Sr contents and lowest Yb contents. The monazite hosted in fenite, ankerite–siderite carbonatite and magnetite–biotite dykes tends to have higher HREE contents and lower Sr contents (ESM1, Fig. S3d). Lead correlates strongly with Th and is typically present at the hundreds of µg/g level but may be up to 8000 µg/g (ESM 2, Table S3). Uranium contents in monazite range from 1 to 90 µg/g (ESM 2, Table S3) and show little correlation with Th or Pb.

Normalised REE + Y (herein REY) plots from in situ LA-ICP-MS analyses show that monazite has two main patterns: (1) relatively straight and flat to downward slopes from La to Sm as illustrated by the monazite in ankerite–siderite carbonatite, alkaline amphibole–dolomite veinlets and some magnetite–biotite dykes (Fig. 6a–c) and (2) curved, positive slopes from La to Pr and/or Nd, followed by an inflexion and gentle, negative slopes from Sm to Gd, as seen in some of the magnetite–biotite dykes and fenitised granite monazite samples (Fig. 6c, d). All samples display a steep, negative slope from Gd to Lu with a small, negative Y anomaly. REY patterns for the magnetite–biotite dyke samples show shifts in the normalised La and Nd contents and variable HREE concentrations (Fig. 6c). The differences in La and Nd contents and the first REY tetrad (La to Nd) for the magnetite–biotite dykes (Fig. 6c) are similar to those changes observed regionally in the REY patterns from the bulk–rock ore samples as discussed below (Fig. 6e). The fenite-hosted monazite has relatively high contents of MREE, yielding arcuate REY patterns (Fig. 6d).

Rhabdophane mineral chemistry

The amorphous to acicular mineral mantling monazite found in the ironstone samples is identified as rhabdophane (Fig. 4c, d). Rhabdophane has high Ca contents (~2.5 to ~

5.5 wt.% CaO; ESM 2, Table S2) and features a negative correlation between Th + Ca and the total measured REY contents. Rhabdophane analyses return low totals (ESM2, Table S2), which are attributed to the incorporation of water into the crystal structure. There is a strong correlation between Nd, Pr and Sm contents, but no correlation between Nd, La or Ce. Furthermore, the La/Nd ratio is similar to that of monazite analysed in the same sample. The Y contents are low and there is little correspondence between REE + P and Th + Si.

Regional variation in REY geochemistry

Regional REY trends are best represented by the bulk-rock geochemistry of drill assays as this dataset has broad spatial coverage of the Yangibana district (Fig. 1) and the bulk-rock REY patterns are primarily dictated by the major ore mineral,

monazite. All prospects are especially enriched in REE (Fig. 6e) and have similar MREE and HREE patterns with small negative Y anomalies. However, there are significant variations in the first tetrad (La to Nd) between the different regions in the district (Fig. 6e). The prospects along the Northern Line show $La_{cn} > Nd_{cn}$, resulting in more flat-lying REY patterns, whereas the other regions show $La_{cn} < Nd_{cn}$, creating a convex upward curve in the REE (Fig. 7a). Moving east along the Northern Line away from Yangibana North, prospects (e.g. Kane's Gossan) show decreasing La_{cn}/Nd_{cn} (Fig. 1b), resulting in a more curved first tetrad (Fig. 6e).

Assay data from all prospects and deposits show a consistent range in La/Nd ~ 0.2 to 1.5 when the total REY $\leq 800 \mu\text{g/g}$ (Fig. 7). The Yangibana North and West deposits from the Northern Line show a higher density of La/Nd values from ~ 0.75 to 1.5 and total REY contents below

Fig. 4 **a** Backscattered electron (BSE) image of monazite from a magnetite–biotite dyke near Fraser's with patchy, dark zonation in large, tabular monazite crystals. Zones are related mainly to changes in Th content (determined by EDS). **b** BSE image of monazite from Yangibana North with oscillatory zoning on the crystal margins. **c** BSE image of fractured monazite altered to slightly darker rhabdophane in a drill cutting sample from Fraser's ironstone. **d** BSE image of radial fibrous rhabdophane in a Fraser's deposit ironstone sample with boxwork texture Fe oxides. **e** False colour (blue = 449–549 nm, green = 553–638 nm, and red = 771–912 nm) hyperspectral cathodoluminescence image of monazite showing slightly patchy texture. The brighter pink colour highlights the prominence of the 857 nm peak from Nd^{3+} in the sample. **f** Spectral image of light and dark zones in the monazite. Both zones have the same patterns, but darker zones have lower counts related to slight changes in REE content

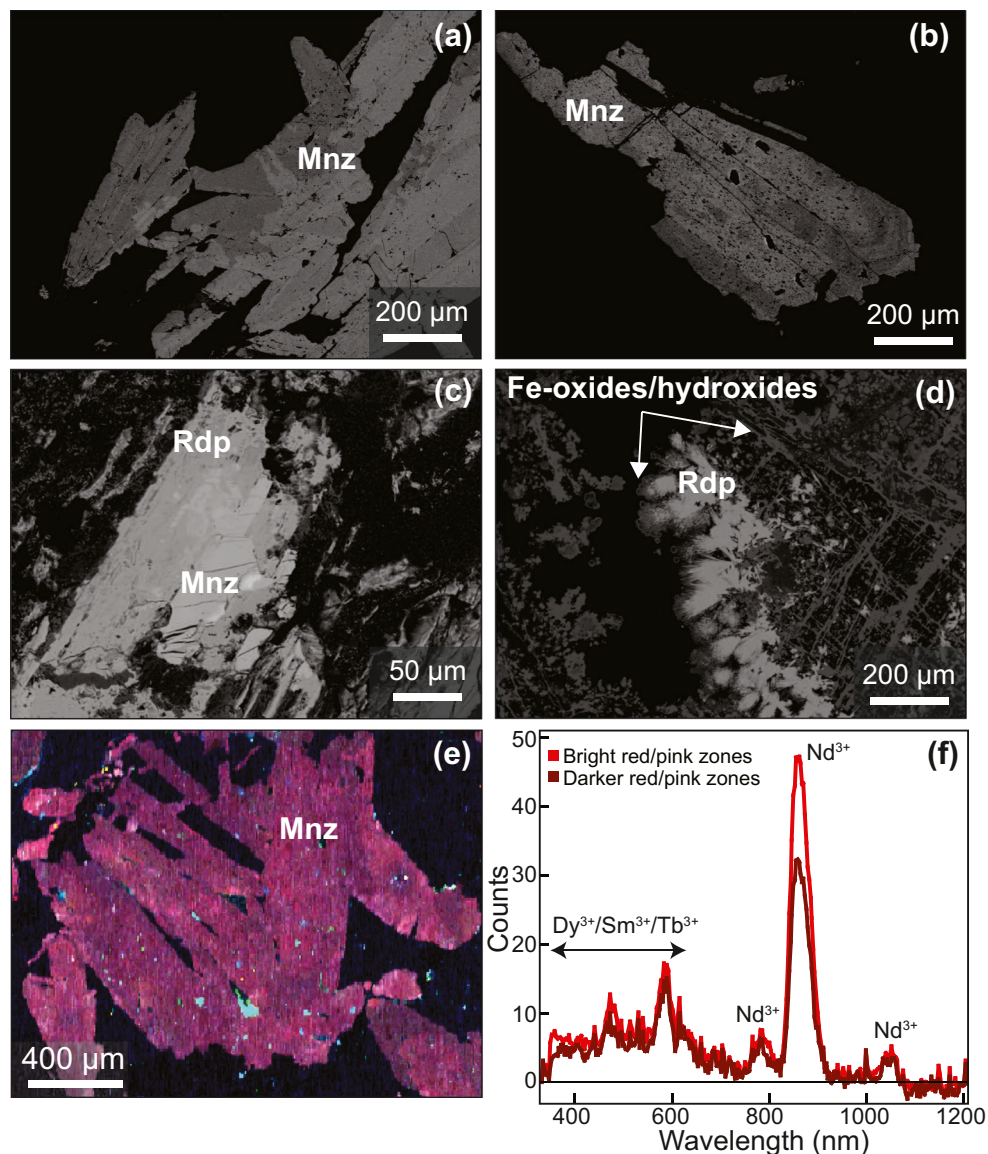
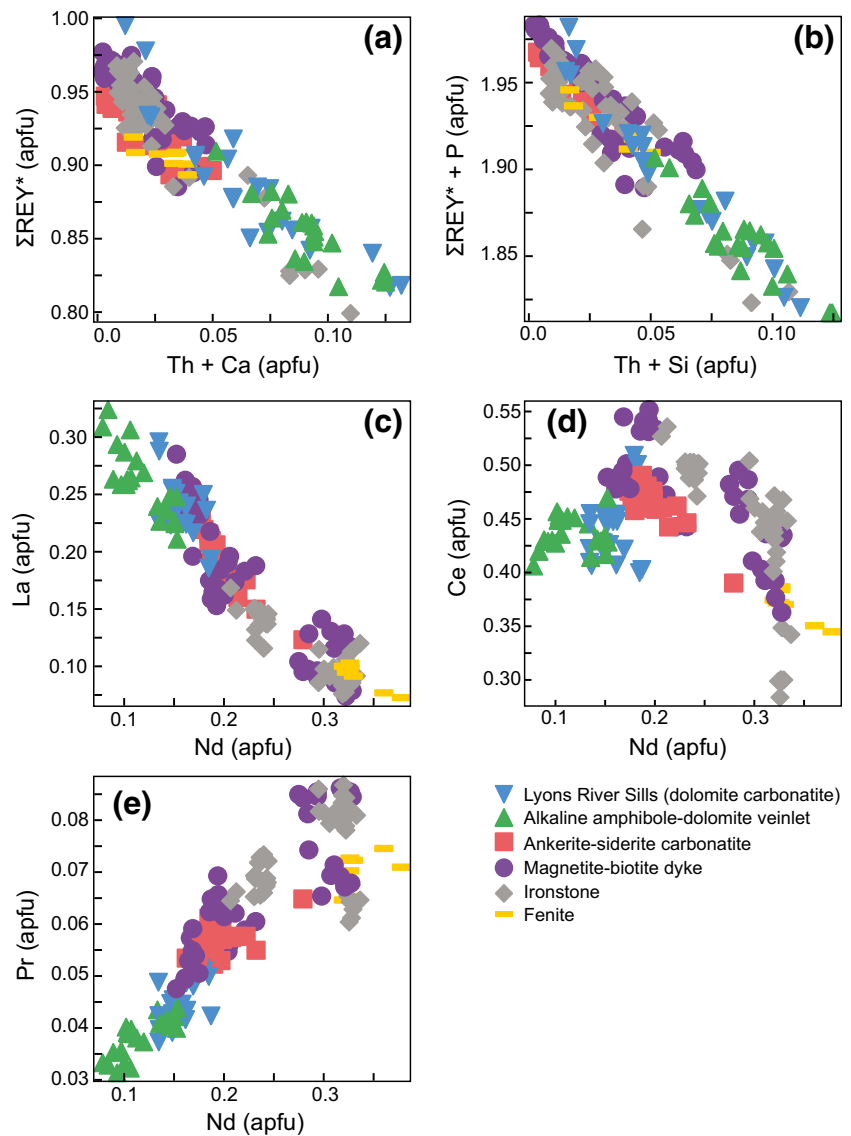


Fig. 5 a–e Atoms-per-formula-unit (apfu) plots (from EPMA analyses) of monazite from various rock types. REY* = La–Sm, Y, and, for some samples, Dy and Gd (see ESM2, Table S2 for details). Note the concentrations in Dy and Gd do not significantly increase the total REY contents in these monazite analyses



800 μg/g (Fig. 7a) compared to the other regions. The deposits and prospects from the other regions have a larger proportion of La/Nd values between ~0.1 and ~0.5 (Fig. 7b–e) and overall higher total REY contents ranging from ~800 μg/g up to 10,000 μg/g (Fig. 7b–e). The general trend for most regions of the GCCC (Fig. 7f) is that as total REY contents increase, the La/Nd ratio decreases.

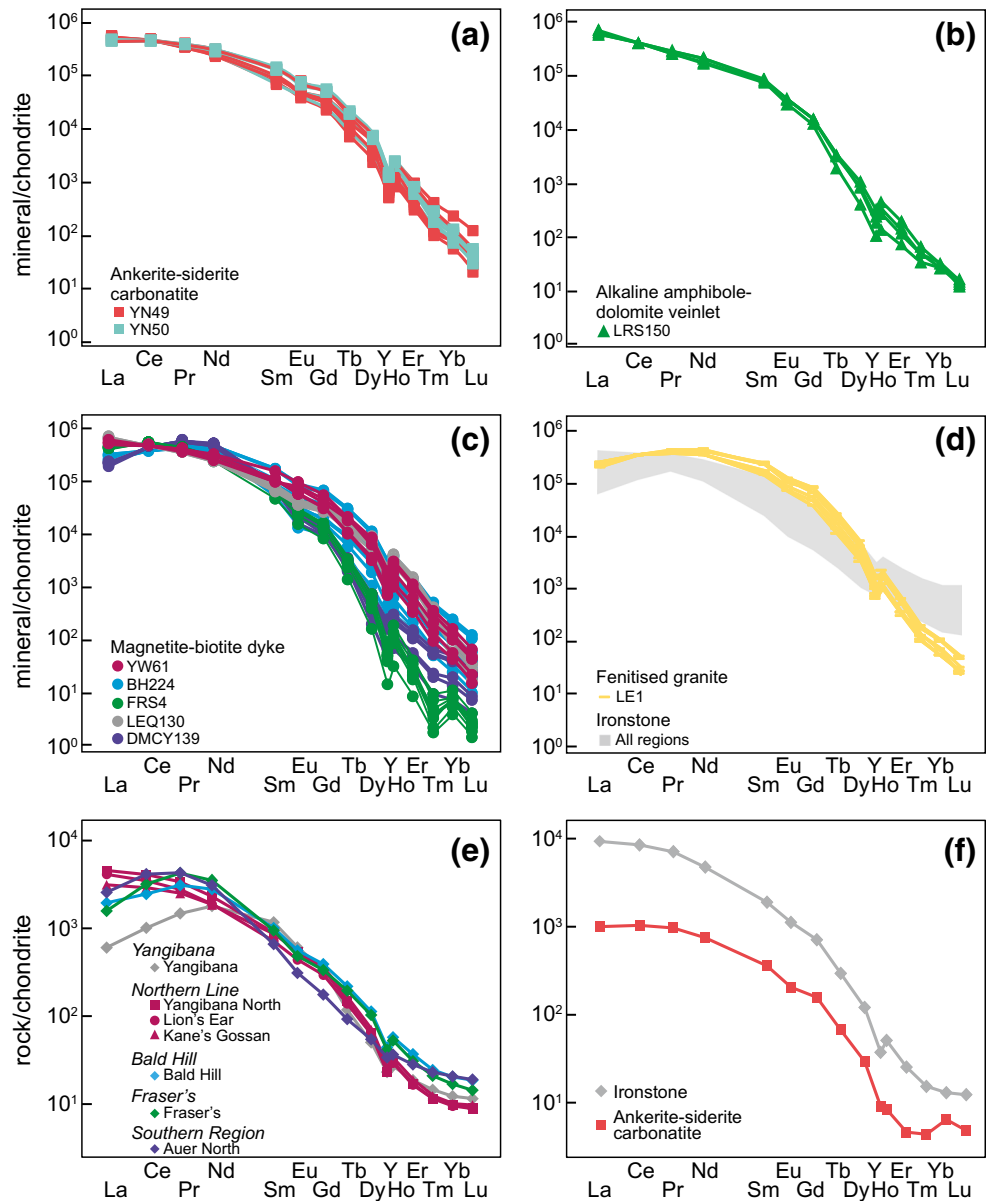
Ironstones compared to least-altered host rocks

Sampling transects were conducted across three different ironstone outcrops (Fig. 1a) hosted within three different country rock types. In all three transects, REE and P₂O₅ contents are highest in the ironstones, demonstrating that the REE phosphate mineralisation is directly associated with the ironstones. The REE mineralisation extends, to a minor extent, into the most proximal fenite halos, and the fenite alteration signatures approach those of the

background host rocks after a relatively short distance (e.g. ~1–2 m). A summary comparing the ironstone, fenite and host rock chemistry is provided in Fig. 8. The complete geochemical data are presented in ESM 2, Table S1.

The ironstone samples have lower SiO₂, MgO, Al₂O₃, Na₂O and K₂O contents, but much higher MnO, P₂O₅ and Fe₂O₃ levels compared to the least-altered host rocks samples (Fig. 8a–d). The granite-hosted (Fraser’s) and schist-hosted ironstone samples have lower TiO₂ contents compared to the least-altered samples, but the quartzite-hosted ironstone in the Edmund Group has higher TiO₂ contents compared to both the unaltered quartzite and other ironstone samples (Fig. 8e). The ironstone samples contain higher Be, Ni, Cu, Zn, Ge, Mo, Sr, REE, Pb, Th and U contents (Table S1) than the fresh and altered rock in which they intrude. Overall, the ironstone samples have lower Cs, Rb and in the granite-hosted ironstones, Ta, compared to the least-altered host rocks.

Fig. 6 Chondrite-normalised REY plots (McDonough and Sun 1995) with REY spacing according to their ionic radius (Shannon 1976). **a** Monazite in ankerite–siderite carbonatite. **b** Monazite in alkaline amphibole–dolomite veinlets. **c** Monazite in magnetite–biotite dykes expressing variation across prospects/deposits. **d** Monazite in fenitised granite and ironstones from across the district. **e** REY patterns for bulk–rock assay data from the different regions in the GCCC (Fig. 1b). Prospect/deposits from the Northern Line contain the highest La_{cn} values, whereas other regions have relatively high Pr_{cn} and Nd_{cn} values. The Northern Line shows a decrease in La_{cn} contents moving east with (the easternmost) Kane’s Gossan having lower La_{cn}/Nd_{cn} compared to (the westernmost) Yangibana North. **f** REY patterns for an average ankerite–siderite carbonatite (from Yangibana North) and an average Yangibana North ironstone. Line data for **a–d** is from in situ LA-ICP-MS analyses on monazite. The monazite values for the ironstones in **d** were calculated from bulk–rock assays assuming all the REE + P are hosted in monazite



Moving away from the ironstones, the fenites show an increase in major elements such as SiO_2 and Na_2O ; however, the concentrations of these oxides are typically less than the least-altered host rocks (Fig. 8a, b). Other components such as Fe_2O_3 , P_2O_5 and Nd decrease in concentration in the fenites moving away from the ironstones (Fig. 8c–f). Oxides and elements such as TiO_2 , Nb and Ta decrease in concentration as the distance from the ironstones increases. Other HFSE elements such as Zr and Hf vary within the fenite samples.

Mass balance calculations and isocon diagrams were used to compare unaltered ankerite–siderite carbonatite drill core samples (e.g. YN50-49, YN49-58 and YN50-48 from Slezak and Spandler 2020) and an average of the ironstone drill samples, using the 51 samples containing > 40 wt.% Fe,

at the Yangibana North prospect. This comparison was conducted as textural and field evidence indicates that the ankerite–siderite carbonatites alter to ironstone (Figs. 2c and 3c, d). The elements Nb, Ta and Zr formed a linear array and are considered to be immobile during low-temperature alteration (MacLean and Kranidiotis 1987), so these elements were chosen to define the isocon (Grant 1986). This isocon has a slope $\sim 7.5:1$ (Fig. 9), indicative of $\sim 85\%$ loss of mass during alteration of the ankerite–siderite carbonatites to REE ore ironstones. The REE and other elements such as Ba, Pb and Th also plot near the isocon (Fig. 9). Major oxides such as MnO , MgO , CaO and Fe_2O_3 plot well to the right of the isocon (Fig. 9), indicating these elements (along with CO_3^{2-}) were removed during conversion of ankerite–siderite carbonatite to ironstone.

Chondrite-normalised REY patterns were plotted for the average ankerite–siderite carbonatite (Slezak and Spandler 2020) and an average of ironstone drill samples from Yangibana North (Fig. 6f). The ironstones contain nearly an order of magnitude greater concentrations of REY compared to the ankerite–siderite carbonatites, but both have similar overall shapes with relatively flat to slightly arcuate patterns from La to Nd followed by steep downward slopes to Ho where the patterns become more flat-lying (Fig. 6f). Of note, the ironstones also have a small but distinct negative Y anomaly.

Sm–Nd isotopes

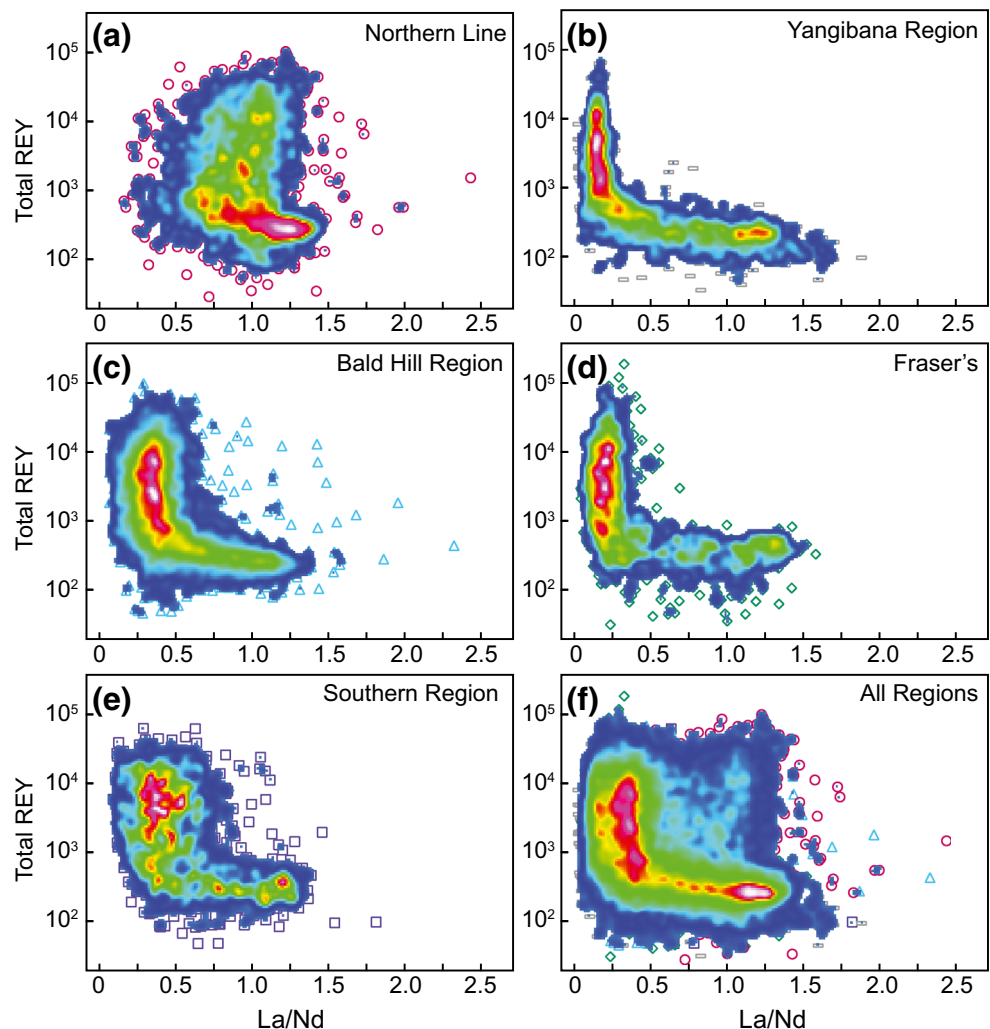
Five bulk-rock samples (three ironstones, one fenite, one Pimbyana Granite) were analysed for Sm–Nd isotope ratios. A summary of the results is presented in Table 1. The ironstone samples have low $^{147}\text{Sm}/^{144}\text{Nd}$ ratios (~ 0.06 to ~ 0.08) compared to the Pimbyana Granite and fenitised Pimbyana Granite samples (~ 0.1). The ironstones from Fraser’s, Lion’s Ear and Yangibana North have $\epsilon\text{Nd}(t_{1.37\text{Ga}})$ values of

-1.55 , -1.83 and -3.24 , respectively. The bulk-rock Nd isotope measurements fall within the range of bulk-rock $\epsilon\text{Nd}(t_{1.37\text{Ga}})$ values (-0.55 to -4.20) for the Lyons River Sills, magnetite–biotite dykes and silica-rich alkaline dykes (Pearson 1996; Slezak and Spandler 2020). The fenitised Pimbyana Granite sample has a fenitisation age $\epsilon\text{Nd}(t_{1.37\text{Ga}})$ of -2.26 , or a granite crystallisation age $\epsilon\text{Nd}(t_{1.68\text{Ga}})$ of 1.27 compared to unaltered Pimbyana Granite which has an $\epsilon\text{Nd}(t_{1.37\text{Ga}})$ of -9.93 , or $\epsilon\text{Nd}(t_{1.68\text{Ga}})$ of -6.07 .

Discussion

Based on petrology, geochemistry and isotopic systematics, the GCCC is considered to have formed via emplacement of evolving, mantle-derived, alkaline magma at mid to upper crustal levels (Slezak and Spandler 2020). The variation in rock types across the complex is interpreted to reflect magma evolution via fractionation (with or without liquid immiscibility), melt wall–rock reaction and hydrothermal alteration

Fig. 7 Density plots of all REY assays for 1 m composites of drill core or chip samples from representative prospects of the different regions in the Yangibana REE district. White, pink and red (i.e. warm colours) represent a high density of datapoints, while cooler colours (e.g. blue) represent a low datapoint density. **a** Yangibana North and Yangibana West. $n = 2869$. **b** Yangibana Region represented by Yangibana and Yangibana South prospects. $n = 1638$. **c** Bald Hill region represented by the Bald Hill deposit. $n = 5262$. **d** Fraser’s region/deposit sample data: $n = 1504$. **e** Southern Region. $n = 2061$. **f** Overlay of all zones showing the regional trend of La/Nd vs. total REY. See Fig. 1 for deposit/prospect locations. Data provided by Hasting Technology Metals Ltd.



(Slezak and Spandler 2020). The REE-rich ironstones of the Yangibana District have spatial associations (Figs. 2c and 3c, d) and similar Nd isotopic compositions to these alkaline igneous rocks, which this study incorporates into a new genetic model (Fig. 10).

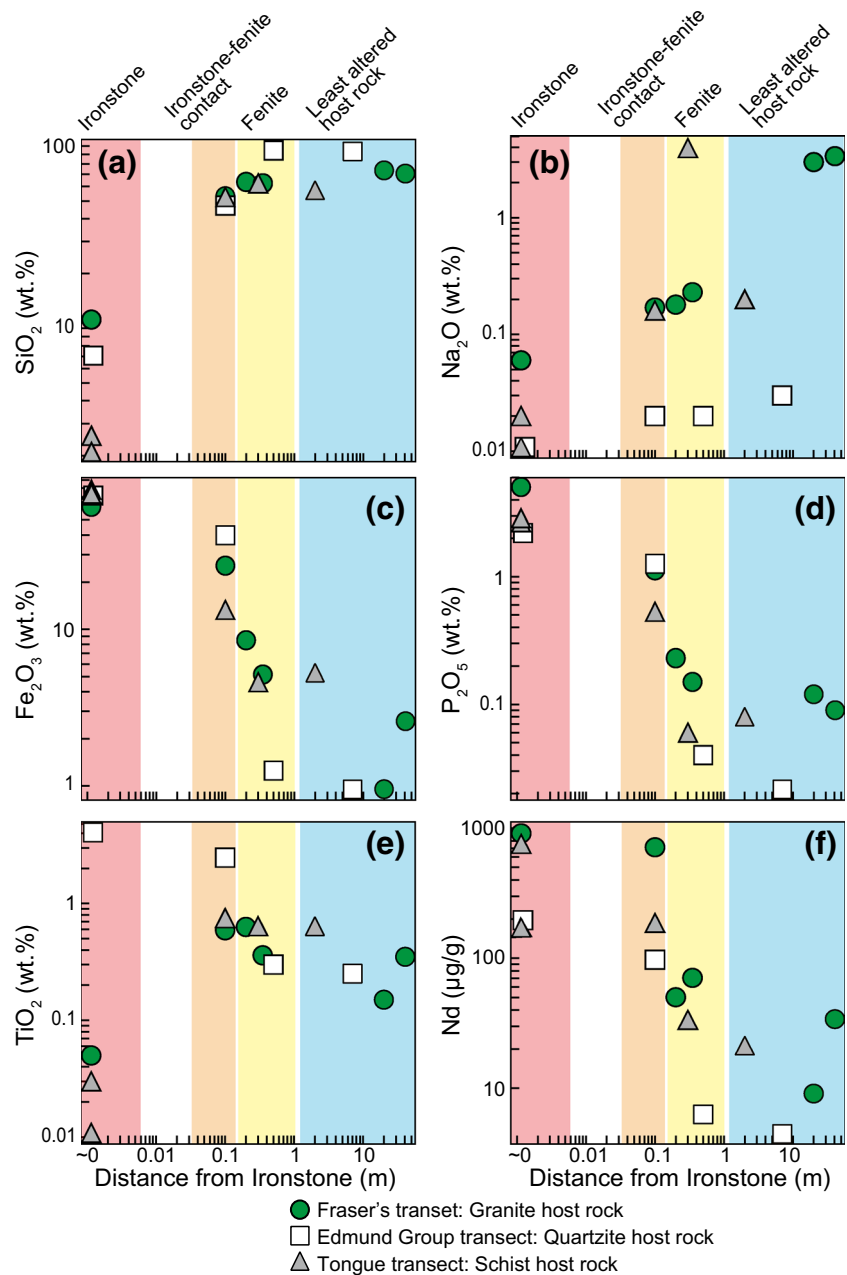
Tectonic and structural conditions of emplacement of the GCCC

Zircon U–Pb dating demonstrates that the GCCC was emplaced c. 1370 Ma in a singular magmatic event (Slezak and Spandler 2019). Subsequent to emplacement, the complex underwent multiple tectonic re-working events as

demonstrated by the various monazite U–Pb and Sm–Nd ages (Zi et al. 2017; Slezak and Spandler 2019). Many carbonatite and alkaline igneous provinces are interpreted to be the result of mantle plume activity (Ernst and Bell 2010; Pirajno 2015). However, this magmatic event does not correlate with any known tectonic event in the Gascoyne Province nor does it spatially correlate with known mantle plume activity, such as the plume-related magmatism in North America and central Africa ~ 1380 Ma (Ernst 2014).

The W to NW orientation of many of the units—subparallel to the Lyons River Fault and Bald Hill Lineament—suggest extension/transtension in the N to NE directions to allow for dyke emplacement along the pre-

Fig. 8 a–f Transect geochemical data (sample locations in Fig. 1a). All concentration values are plotted against distance (log scale) from the ironstone



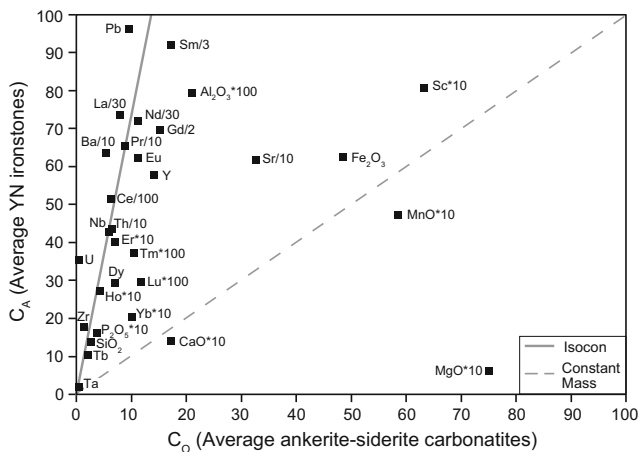


Fig. 9 Isocon diagram comparing the average of the least-altered ankerite–siderite carbonatite samples (Yangibana North area) to an average Yangibana North ironstone, based on bulk–rock assays from Hastings Technology Metals Ltd. The isocon is defined by Nb, Ta and Zr

existing structures. The step-over veins (ESM1, Fig. S1), orthogonal orientation of the GCCC units (Fig. 1) and close correlation between dyke morphology and pre-existing structures (Fig. 1 and ESM 1, Fig. S1) indicate that the area was subjected to extensional stresses, which allowed the low viscosity carbonatite melts to permeate the crust. Neither extensive brecciation/explosive features nor intrusive plugs are observed in the GCCC, which, together with the prevalence of fine-grained dyke morphologies, suggest a hypabyssal emplacement setting (Barker 1989). Carbonatite melts typically have low viscosities (Treiman 1989) and, in the case of the GCCC, may also be of small volumes. These features may be why the GCCC occurs as relatively thin dykes and sills along pre-existing structures, rather than as substantial intrusive plugs or volcanic pipes. Vaughan and Scarrow (2003) demonstrated that lithospheric transtensional faulting may trigger localised mantle magmatism, and work by Jelsma et al. (2004)

showed that large regional structures act as emplacement corridors for small volume, mantle-derived melts. A similar scenario is proposed whereby the Lyons River Fault underwent extension/transension at c. 1370 Ma, allowing for the migration of alkaline melts from the mantle to hypabyssal emplacement into the crust, forming the GCCC (Slezak and Spandler 2020). Motion along the Lyons River Fault may have been caused by far-field stresses related to the separation of the North China Craton from the West Australia Craton around 1400 to 1350 Ma (Pisarevsky et al. 2014; Slezak and Spandler 2019, 2020) or by far-field stresses related to the incipient convergence of the Mawson Craton with the southeastern margin (present day) of the West Australia Craton (Aitken et al. 2016; Stark et al. 2018).

Ore mineral chemistry and REE trends

Monazite in the Yangibana REE district luminesces in the infrared spectrum with peaks at approximately 784 nm, 857 nm and 1048 nm (Fig. 4f); these peaks have been shown to be associated with Nd³⁺ (Richter et al. 2008; Lenz et al. 2013; Gaft et al. 2015). Other small peaks near 474 nm and 583 nm with elevated counts down to 350 nm are most likely associated with Dy³⁺, Sm³⁺, and/or Tb³⁺ (Gorobets and Rogojine 2001; Richter et al. 2008). Variation in the CL intensities in the dark and light pink zones (in the false colour maps) are related to varying REE contents, particularly Nd³⁺, which can be seen in the variations in the 857 nm peak (Fig. 4f).

Though low in overall Ca and Si contents, the monazite in the Yangibana REE district shows strong correlations between Th, Si, Ca, REE and P, indicative of the common coupled substitutions of Th⁴⁺ + Ca²⁺ = 2REE³⁺ and Th⁴⁺ + Si⁴⁺ = REE³⁺ + P⁵⁺ related to cheralite and huttonite solid solutions, respectively (Fig. 5a, b; Gramaccioli and Segalstad 1978; Van Emdem et al. 1997). The high Sr content of monazite from the alkaline amphibole–dolomite veinlet is likely due to Sr²⁺

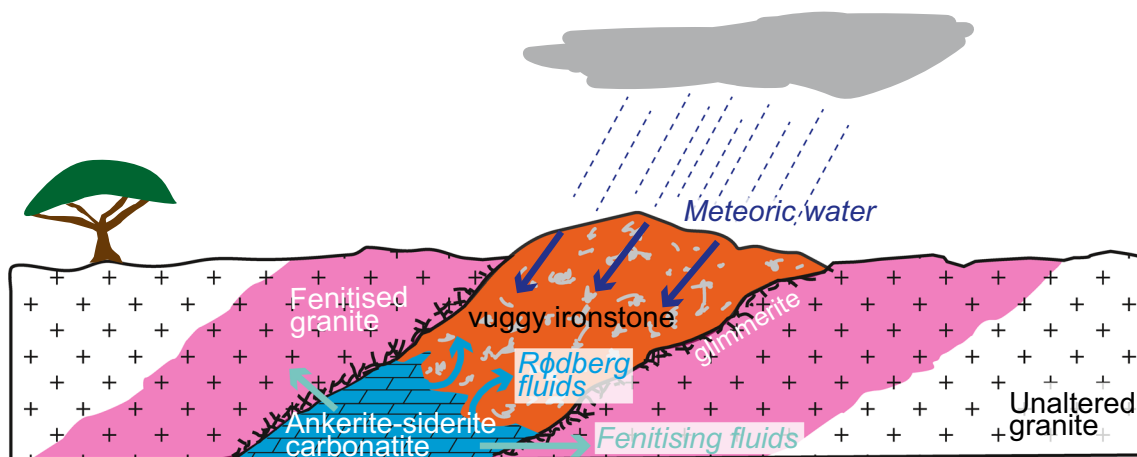


Fig. 10 Schematic of ironstone formation via alteration of the ankerite–siderite dykes by rødberg and meteoric water. Associated fenites and glimmerites are also shown

cheralite-type substitution (Wall and Zaitsev 2004), which can be attributed to the higher Sr contents in the Lyons River Sills (Slezak and Spandler 2020). The correlation between As and Nd is likely related to the presence of AsO_4^{3-} , which can substitute for PO_4^{3-} (Clavier et al. 2011).

Lanthanum and Nd show an intriguing inverse relationship where monazite from the Lyons River Sills and their associated alkaline amphibole–dolomite veinlets have high $\text{La}_{\text{cn}}/\text{Nd}_{\text{cn}}$ (Fig. 6b) compared to other rock types, which show increasing Pr, Nd and Sm (Fig. 5c, e) contents with decreasing La contents. This relationship between La and Nd is also reflected in the REY normalised apatite patterns (Slezak et al. 2018) and appears as a pivot around Ce in the chondrite-normalised plots for the magnetite–biotite dykes (Fig. 6c). In addition, there are regional variations in $\text{La}_{\text{cn}}/\text{Nd}_{\text{cn}}$ (Fig. 1b) that are reflected in the mineralisation, showing the ore from the Yangibana, Bald Hill, Fraser’s and Southern Regions tends to be more enriched in Nd (Figs. 6e and 7).

The shift from La to Nd enriched carbonatite phases has been documented in the Khibina carbonatites (Russia) and Bear Lodge carbonatite (USA) by Zaitsev et al. (1998) and Moore et al. (2015), respectively. Both studies observed higher Nd contents in REE carbonate minerals, which the authors surmised were indicative of more evolved units. In addition, high Th contents in monazite are indicative of higher formation temperatures (Wall and Zaitsev 2004). The monazite in the Lyons River Sills and their associated alkaline amphibole–dolomite veinlets has much higher Th, Sr and La contents compared to monazite occurring in the other rock types (Fig. 5a–c and ESM 1, Fig. S3c, d), which suggests these units may have formed early during the emplacement of the GCCC. Slezak and Spandler (2020) postulated the higher Fe contents, observed in the magnetite–biotite dykes and ankerite–siderite carbonatite, suggest these units may be paragenetically later and more evolved than the Lyons River Sills, an observation that is corroborated by the Nd-rich monazite.

In addition to magmatic effects on REE distribution, the variation between La and Nd may be related to REE uptake related to sector zoning in the monazite crystal structure (Cressey et al. 1999), which in turn may reflect hydrothermal processes in the carbonatite system such as changes in fluid type and temperature (Smith et al. 2000; Wall and Zaitsev 2004; Migdisov et al. 2016; Chen et al. 2017). Changes in fluid type (i.e. CO_2 vs. H_2O) can contribute to REE fractionation within a system, affecting element availability during monazite crystallisation. In the monazite–aegirine hydrothermal veins at Bayan Obo, high La values in monazite were regarded to be indicative of greater La (and Ce) solubility in CO_2 -rich fluids compared to Nd and Sm, which were more likely to be associated with aqueous fluids (Smith et al. 2000). The bulk-rock REY patterns of the ironstone from Lion’s Ear

prospect show $\text{La}_{\text{cn}} > \text{Nd}_{\text{cn}}$ (Figs. 1b and 6e), whereas the monazite REY patterns from Lion’s Ear fenite sample (LE1) display greater curvature in the first tetrad with $\text{La}_{\text{cn}} < \text{Nd}_{\text{cn}}$ (Fig. 6d). This change could be linked to a switch from a CO_2 -rich magmatic-hydrothermal system (i.e. ankerite–siderite carbonatite) towards an H_2O -dominated, fenitising fluid and/or a decrease in the fluid temperature as the fluids infiltrate the cold granite host rock (Smith et al. 2000; Migdisov et al. 2016).

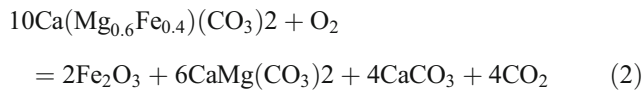
Migdisov et al. (2016) demonstrated that REE was more mobile than HREE at lower hydrothermal temperatures and that REE could also be variably fractionated based on solubility in the presence of F- and Cl-bearing fluids, the latter providing more effective transport mechanisms for REE. Chlorine contents in biotite from the ankerite–siderite carbonatites are higher than biotite from other units (Slezak and Spandler 2020); the higher Cl in the ankerite–siderite carbonatites may have contributed to fractionated REE contents (Migdisov et al. 2016) in these rocks and their alteration products.

Origins of the ironstone

The bulk-rock chemistry of the ironstones is very different from the other rock types found in the complex, as they are almost entirely composed of Fe_2O_3 and SiO_2 with subordinate phosphate mineralisation. The geochemical transects across the ironstones into the country rock show the ironstones contain higher amounts of elements common to alkaline magmatic systems such as REE, P, Th and U (Fig. 8; Woolley and Kempe 1989) in contrast to the rocks in which they intrude (i.e. quartzite, pelitic schist and granite). The ironstones are also enveloped by fenite and glimmerite alteration halos analogous to those observed around the ankerite–siderite carbonatites and Lyons River Sills (e.g. Fig. 3f). In addition, the ironstones have bulk-rock Nd isotope compositions (Table 1) that are similar to other units of the GCCC (Slezak and Spandler 2020), indicating they have a common (enriched mantle) source. The Pimbyana Granite $\epsilon\text{Nd}(t_{1.37\text{Ga}}) = -9.93$ than the fenitised granite samples ($\epsilon\text{Nd}(t_{1.37\text{Ga}}) = -2.26$), demonstrating that REE were added to host rocks during fenitisation.

The observation of carbonate mineral dissolution cavities and ankerite–siderite carbonatite altering to ironstone-like rocks are consistent with the original hypothesis of Gellatly (1975) that the ironstones are likely the product of dissolution of carbonate minerals. Pearson et al. (1996) indicated that the ironstones may be analogous to “rødberg”, an iron-rich, low temperature, calcite–dolomite–iron oxide rock that forms as a result of metasomatism from hydrothermal fluids (Andersen 1984; Le Bas 1989). The rødberg rocks, originally described in the Fen Complex (Norway), were formed by low temperature (200 to 300 °C) hydrothermal, oxidising fluids above the

haematite-magnetite buffer, which altered the ankerite–siderite carbonatites to calcite, dolomite and haematite via the following reactions as described by Andersen (1984):



The textures reported included intergrowths of calcite and dolomite, fine-grained platy haematite and resorption features in ankerite (Andersen 1984). In the GCCC, Pirajno and González-Álvarez (2013) observed haematite development along carbonate lamellae, and haematite veins cross-cutting other textures, both of which were interpreted as higher-temperature rødberg-style reactions. These distinct, euhedral crystal features of haematite were not observed in this study. However, in some ankerite–siderite carbonatite samples, magnetite–biotite veins cross-cutting the fresh ankerite–siderite carbonate were observed in close proximity to oxidised zones comparable to the ironstones (Fig. 3c). Marien et al. (2018) reported phlogopite-bearing veins as a component of in the transitional rødberg zones. Additionally, sparry carbonate crystals—likely calcite—mantle large monazite crystals (Fig. 3e) in similar zones and indicate an early hydrothermal component in the formation of the ironstones at Yangibana. As these observations are rare in the ironstone, it is speculated that much of these higher-temperature alteration characteristics have been overprinted by low-temperature meteoric features such as botryoidal haematite, boxwork textures (Fig. 4d) and vugs (Fig. 3b).

The transformation of monazite to rhabdophane (Fig. 4c,d) occurs under low-temperature hydrothermal conditions, as rhabdophane is only stable at $T < 400$ °C at 0.05 GPa and $T < 200$ °C at 0.1 GPa (Akers et al. 1993). Rhabdophane has also been reported to form at temperatures as low as 5 °C and under acidic, REE-saturated fluid conditions (Roncal-Herrero et al. 2011), suggesting a temperature range consistent with hydrothermal and meteoric origins. Based on the available textural and mineralogical evidence, the ironstones likely formed by partial rødberg-style alteration of the ankerite–siderite carbonatites and possibly magnetite–biotite dykes, which was subsequently overprinted by meteoric water (Fig. 10), which dissolved the carbonate mineral phases and precipitated low-temperature goethite, haematite, other Fe–Mn oxides/hydroxides and silica (Pirajno and González-Álvarez 2013; this study).

The West Australia Craton has episodically undergone subaerial exposure since the late Proterozoic, though much of it underwent extensive regolith development from the Paleogene until the mid-Miocene (Anand and Paine 2002; Pillans 2007). The extended length of subaerial exposure of the GCCC has provided ample time for meteoric water to infiltrate and alter the dykes, forming the present-day

ironstones (Fig. 10). This is supported by ankerite–siderite carbonatite altering to ironstone in core samples (Figs. 2c and 3c, d) and unaltered ankerite–siderite carbonatite only occurring in drill core from depths ≥ 40 m below the areas where the ironstones crop out at the surface. The depth of meteoric fluid infiltration was likely controlled and/or enhanced by porosity generation via carbonate dissolution and joints, faults or wall–rock contacts in the carbonatites.

Ironstone REE ore genesis

Weathering and laterite formation are important processes that can improve the ore tenor of carbonatite deposits. The largest Nb deposits in the world occur in Brazil and include the pyrochlore-rich carbonatite deposits Araxá, Catalão and Morro do Seis Lagos, which have all undergone extensive lateritisation (Chakhmouradian et al. 2015; Mitchell 2015; Giovannini et al. 2017). The laterites mainly increase the Nb ore tenor by weathering through eluvial enrichment where carbonate minerals are dissolved or remobilised, leaving the immobile pyrochlore as residual material (Mariano 1989). By contrast, the primary REE-bearing minerals (REE(fluor)carbonates and REE phosphates) at Araxá and Catalão I are dissolved in the supergene environment, liberating REE, which are then incorporated into Al-phosphates such as gorceixite and, to a lesser extent, bound to Fe hydroxides (Morteani and Preinfalk 1996).

Extensive supergene enrichment of REE via lateritisation has also occurred at the Mount Weld and Bear Lodge carbonatites, where breakdown of primary REE-bearing minerals (e.g. monazite, apatite, ancyllite) has liberated REE to form REE-bearing oxyhydroxides, REE(fluor)carbonates, secondary monazite, churchite, cerianite and REE-rich hydrated aluminophosphate (plumbogummite group) minerals (Lottermoser 1990; Moore et al. 2015; Andersen et al. 2017). This lateritisation has enriched LREE concentrations by ~ 5 to 200 times compared to the average carbonatite LREE contents (Lottermoser 1990; Andersen et al. 2017).

Comparison of the Yangibana ironstones with likely precursor ankerite–siderite carbonatite (Fig. 6f) indicates an average upgrade in ore tenor of ~ 2 to ~ 10 times during supergene alteration. Overall, the ankerite–siderite carbonatite and ironstones have comparable normalised REY patterns (Fig. 6f), which is consistent with their genetic relationship and indicative of an environment involving little fractionation between REE (Morteani and Preinfalk 1996). This is in contrast with the Mount Weld and Bear Lodge deposits where laterite formation was accompanied by variable fractionation of LREE/HREE and development of Ce anomalies in REE minerals due to differential transport of oxidised Ce^{4+} for other trivalent REE (Lottermoser 1990; Andersen et al. 2017). The ironstones of the Yangibana REE district demonstrate that some monazite has been altered and remobilised to form rhabdophane and possibly REE-bearing Fe oxides/

hydroxides, similar to the processes at Araxá, Catalão I and Mount Weld. However, most of the monazite in Yangibana is interpreted to be primary, with relative monazite enrichment occurring through eluvial supergene processes, as opposed to the dissolution and re-precipitation of REE minerals under hydrothermal and/or meteoric conditions (Morteani and Preinfalk 1996). This may explain the paucity of secondary REE minerals, such as REE-(fluor)carbonates or REE alumina-phosphates, and lack of REE fractionation at Yangibana in comparison to other lateritic REE deposits, such as Mount Weld and Bear Lodge. The lack of REE mobility and redistribution at Yangibana may in part be due to the relatively simple Fe-rich composition of the host rock, but more importantly is likely due to the primary monazite mineralogy compared to other carbonatite complexes where apatite and carbonates are the primary REE host minerals (Lottermoser 1990; Andersen et al. 2017). Monazite is expected to be significantly less soluble than apatite or carbonates in meteoric water (Janots et al. 2008), which may have inhibited REE mobility during laterite formation at Yangibana. In this sense, ore formation processes at Yangibana have closer similarities to those involving pyrochlore concentration in the Araxá, Catalão I, and Morro do Seis Lagos deposits in Brazil (Mariano 1989; Mitchell 2015; Giovannini et al. 2017).

Conclusions

1. The GCCC was emplaced in a transtensional/extensional setting.
2. The REE-rich ironstones are genetically related to the other magmatic units in the GCCC, showing analogous enriched mantle Nd isotope values to the unaltered alkaline intrusive rocks.
3. The spatial variation in La/Nd across the GCCC relates to petrologic differences as well as changes in the magmatic-hydrothermal system with respect to CO₂ and temperature.
4. The ironstones were likely formed by Rødberg-style alteration followed by weathering and oxidation by meteoric water of the ankerite–siderite carbonatite.
5. REY content of the ironstones was enriched ~2 to ~10 times mainly by eluvial supergene processes.
6. The GCCC shows many similarities with other major critical metal-bearing carbonatites such as its tectonic setting, enriched mantle component and increase in ore tenor through weathering and lateritisation.

Acknowledgements We thank Hasting Technology Metals Limited for their sample contributions, drill hole data and hospitality while conducting fieldwork. We also thank Kevin Blake, Shane Askew, Brendan Jones and Yi Hu from the JCU Advanced Analytical Centre for their assistance with the EPMA, XRF and LA-ICP-MS analyses. We thank Kathryn Goodenough; Franco Pirajno; the handling editor,

Robert Linnen; and the editor, Georges Beaudoin, for their reviews, which improved this manuscript.

Funding An ARC Future Fellowship (FT 120100198) to Carl Spandler supported this study.

References

- Aitken ARA, Betts PG, Young DA, Blankenship DD, Roberts JL, Siegert MJ (2016) The Australo-Antarctic Columbia to Gondwana transition. *Gondwana Res* 29:136–152
- Akers WT, Grove M, Harrison TM, Ryerson FJ (1993) The instability of rhabdophane and its unimportance in monazite paragenesis. *Chem Geol* 110:169–176
- Anand RR, Paine M (2002) Regolith geology of the Yilgarn Craton, Western Australia: implications for exploration. *Aust J Earth Sci* 49:3–162
- Andersen T (1984) Secondary processes in carbonatites: petrology of 'rodberg' (hematite-calcite-dolomite carbonatite) in the Fen central complex, Telmark (South Norway). *Lithos* 17:227–245
- Andersen AK, Clark JG, Larson PB, Donovan JJ (2017) REE fractionation, mineral speciation, and supergene enrichment of the Bear Lodge carbonatites, Wyoming, USA. *Ore Geol Rev* 89:780–807
- Armstrong JT (1991) Quantitative element analysis of individual micro-particles with electron beam instruments. In: KFJ H, Newbury DE (eds) *Electron probe quantification*. Plenum Press, New York, pp 261–315
- Barker DS (1989) Field relations of carbonatites. In: Bell K (ed) *Carbonatites: genesis and evolution*. Unwin Hyman, London, pp 38–69
- Chakhmouradian AR, Zaitsev AN (2012) Rare earth mineralization in igneous rocks: sources and processes. *Elements* 8:347–353
- Chakhmouradian AR, Reguir EP, Kressall RD, Crozier J, Pisiak LK, Sidhu R, Yang P (2015) Carbonatite-hosted niobium deposit at Aley, northern British Columbia (Canada): mineralogy, geochemistry and petrogenesis. *Ore Geol Rev* 64:642–666
- Chen W, Honghui H, Bai T, Jiang S (2017) Geochemistry of monazite within carbonatite related REE deposits. *Resources* 6(4):51
- Clavier N, Podor R, Dacheux N (2011) Crystal chemistry of the monazite structure. *J Eur Ceram Soc* 31:941–976
- Cressey G, Wall F, Cressey BA (1999) Differential REE uptake by sector growth of monazite. *Mineral Mag* 63(6):813–828
- Cutten HN, Johnson SP (2018) Kuparr tectonic event (KU): WA geology online, Explanatory Notes Extract. Geological Survey of Western Australia
- Elliott HAL, Wall F, Chakhmouradian AR, Siegfried PR, Dahlgren S, Weatherley S, Finch AA, Marks MAW, Deady E (2018) Fenites associated with carbonatite complexes: a review. *Ore Geol Rev* 98:38–59
- Ernst RE (2014) *Large igneous provinces*. Cambridge University Press
- Ernst RE, Bell K (2010) Large igneous provinces (LIPs) and carbonatites. *Mineral Petrol* 98:55–76
- Fisher CM, McFarlane CRM, Hanchar JM, Schmitz MD, Sylvester PJ, Lam R, Longerich HP (2011) Sm-Nd isotope systematics by laser ablation-multicollector-inductively coupled plasma mass spectrometry: methods and potential natural and synthetic reference materials. *Chem Geol* 284:1–20
- Fricke MB, Kutscher D, Aeschlimann B, Frommer J, Dietiker R, Bettner J, Gunther D (2011) High spatial resolution trace element analysis by LA-ICP-MS using a novel ablation cell for multiple large samples. *Int J Mass Spectrom* 307:39–45

- Gaft G, Reisfeld R, Panczer G (2015) Modern luminescence spectroscopy of minerals and materials. Springer Mineralogy, Cham
- Gellatly DC (1975) Yangibana Creek U-Th-REE-base metal prospect, Gascoyne Goldfield, W.A. Amax Exploration (Australia) Inc
- Giovannini AL, Bastos Neto AC, Porto CG, Pereira VP, Takehara L, Barbanson L, Bastos PHS (2017) Mineralogy and geochemistry of laterites from the Morro dos Seis Lagos Nb (Ti, REE) deposit (Amazonas, Brazil). *Ore Geol Rev* 88:461–480
- Goodenough KM, Schilling J, Jonsson E, Kalvig P, Charles N, Tuduri J, Deady EA, Sadeghi M, Schiellerup H, Müller A, Bertrand G, Arvanitidis N, Eliopoulos DG, Shaw RA, Thrane K, Keulen N (2016) Europe's rare earth element resource potential: an overview of REE metallogenetic provinces and their geodynamic setting. *Ore Geol Rev* 72:838–856
- Gorobets BS, Rogojine A (2001) Luminescent spectra of minerals. RPC VIMS, Moscow (in Russian)
- Gramaccioli CM, Segalstad TM (1978) A uranium-and thorium-rich monazite from a south-alpine pegmatite at Piona, Italy. *Am Miner* 63:757–761
- Grant JA (1986) The isocon diagram—a simple solution to Gresens' equation for metasomatic alteration. *Econ Geol* 81:1976–1982
- Gresens RL (1967) Composition-volume relationships of metasomatism. *Chem Geol* 2:47–65
- Guillong M, Meier DL, Allan MM, Heinrich CA, Yardley BWD (2008) SILLS: a MATLAB-based program for the reduction of laser ablation ICP-MS data of homogenous materials and inclusions. In: Sylvester P (ed) *Laser ablation ICP-MS in the Earth Sciences: current practices and outstanding issues*. Mineralogical Association of Canada, Vancouver, pp 328–333
- Hastings Technology Metals (2019) News: 13% Increase in measured and indicated mineral resources. Retrieved from <https://hastingsstechmetals.com/2019/10/13-increase-in-measured-and-indicated-mineral-resources/> on May 3, 2020
- Jaireth S, Hoatson DM, Miezitis Y (2014) Geological setting and resources of the major rare-earth-element deposits in Australia. *Ore Geol Rev* 62:72–128
- Janots E, Brunet F, Goffé B, Poinssot C, Burchard M, Cemic L (2008) Thermochemical characterization of $\text{Ca}_4\text{La}_6(\text{SiO}_4)_6(\text{OH})_2$ a synthetic La- and OH-analogous of britholite: implication for monazite and LREE apatites stability. *Mineralogia* 39:41–52
- Jelsma HA, de Wit MJ, Thiart C, Dirks PHGM, Viola G, Basson IJ, Anckar E (2004) Preferential distribution along transcontinental corridors of kimberlites and related rocks of Southern Africa. *S Afr J Geol* 107:301–324
- Johnson SP, Sheppard S, Rasmussen B, Wingate MTD, Kirkland CL, Muhling JR, Fletcher IR, Belousova EA (2011) Two collisions, two sutures: punctuated pre-1950 Ma assembly of the West Australian Craton during the Ophthalmian and Glenburgh Orogenies. *Precambrian Res* 189:239–262
- Johnson SP, Thorne AM, Tyler IM, Korsch RJ, Kennett BLN, Cutten HN, Goodwin J, Blay O, Blewett RS, Joly A, Dentith MC, Aitken ARA, Holzschuh J, Salmon M, Reading A, Heinson G, Boren G, Ross J, Costelloe RD, Fomin T (2013) Crustal architecture of the Capricorn Orogen, Western Australia and associated metallogeny. *Aust J Earth Sci* 60:681–705
- Johnson SP, Korhonen FJ, Kirkland CL, Cliff JB, Belousova EA, Sheppard S (2017) An isotopic perspective on growth and differentiation of Proterozoic orogenic crust: from subduction magmatism to cratonization. *Lithos* 268–271:76–86
- Korhonen FJ, Johnson SP, Fletcher IR, Rasmussen B, Sheppard S, Muhling JR, Dunkley DJ, Wingate MTD, Roberts MP, Kirkland CL (2015) Pressure-temperature-time evolution of the Mutherbukin Tectonic Event, Capricorn Orogen. Geological Survey of Western Australia, Report 146, pp 64
- Le Bas MJ (1989) Diversification of carbonatite. In: Bell K (ed) *Carbonatites genesis and evolution*. Unwin Hyman Ltd, London, pp 428–447
- Le Maitre RW (2002) *Igneous rocks: a classification and glossary of terms: recommendations of International Union of Geological Sciences, subcommission on the systematics of igneous rocks*. Cambridge University Press, Cambridge
- Lenz C, Talla D, Ruschel K, Škoda R, Götze J, Nasdala L (2013) Factors affecting the Nd^{3+} (REE^{3+}) luminescence of minerals. *Mineral Petrol* 107(3):415–428
- López-Moro FJ (2012) EASYGRESGRANT—A Microsoft excel spreadsheet to quantify volume changes and to perform mass-balance modeling in metasomatic systems. *Comput Geosci* 39: 191–196
- Lottermoser BG (1990) Rare-earth element mineralisation within the Mt. Weld carbonatite laterite, Western Australia. *Lithos* 24:151–167
- Luo Y, Gao S, Longrich HP, Gunter D, Wunderli S, Yuan H-L, Liu X-M (2007) The uncertainty budget of the multi-element analysis of glasses using LA-ICP-MS. *J Anal Spectrom* 22:122–130
- MacLean WH, Kranidiotis P (1987) Immobile elements as monitors of mass transfer in hydrothermal alteration, Phelps Dodge massive sulfide deposit, Matagami, Quebec. *Econ Geol* 82:951–962
- Mariano AN (1989) Nature of economic mineralization in carbonatites and related rocks. In: Bell K (ed) *Carbonatites genesis and evolution*. Unwin Hyman, London, pp 149–176
- Marien C, Dijkstra AH, Wilkins C (2018) The hydrothermal alteration of carbonatite in the Fen Complex, Norway: mineralogy, geochemistry, and implications for rare-earth element resource formation. *Mineral Mag* 82(S1):S115–S131
- Martin DM, Thorne AM (2004) Tectonic setting and basin evolution of the Bangemall Supergroup in the northwestern Capricorn Orogen. *Precambrian Res* 128:385–409
- McDonough WF, Sun Ss (1995) The composition of the earth. *Chem Geol* 120:223–253
- Migdisov A, Williams-Jones AE, Brugger J, Caporuscio FA (2016) Hydrothermal transport, deposition, and fractionation of the REE: experimental data and thermodynamic calculations. *Chem Geol* 439:13–42
- Mitchell RH (2015) Primary and secondary niobium mineral deposits associated with carbonatites. *Ore Geol Rev* 64:626–641
- Moore M, Chakhmouradian AR, Mariano AN, Sidhu R (2015) Evolution of rare-earth mineralization in the Bear Lodge carbonatite, Wyoming: mineralogical and isotopic evidence. *Ore Geol Rev* 64: 499–521
- Morteani G, Preinfalk C (1996) REE distribution and REE carriers in laterites formed on the alkaline complexes of Araxa and Catalao (Brazil). In: Jones AP, Wall F, Williams CT (eds) *Rare earth minerals: chemistry, origin and ore deposits*. Chapman and Hall, London
- Olierook HKH, Agangi A, Plavska D, Reddy SM, Yao W, Clark C, Occhipinti SA, Kylander-Clark ARC (2019) Neoproterozoic hydrothermal activity in the West Australian Craton related to Rodinia assembly or breakup? *Gondwana Res* 68:1–12
- Pearson JM (1996) Alkaline rocks of the Gifford Creek Complex, Gascoyne Province, Western Australia: their petrogenetic and tectonic significance Department of Geology and Geophysics. PhD thesis. University of Western Australia, pp 462
- Pearson JM, Taylor WR (1996) Mineralogy and geochemistry of fenitized alkaline ultrabasic sills of the Gifford Creek Complex, Gascoyne Province, Western Australia. *Can Mineral* 34:201–219
- Pearson JM, Taylor WR, Barley ME (1996) Geology of the alkaline Gifford Creek Complex, Gascoyne Complex, Western Australia. *Aust J Earth Sci* 43:299–309
- Pettke T (2008) Analytical protocols for element concentration and isotope ratio measurements in fluid inclusions by LA-(MC)-ICP-MS. In: Sylvester P (ed) *Laser ablation ICP-MS in earth sciences: current*

- practices and outstanding issues. Mineral Association of Canada, Vancouver, pp 189–218
- Pettke T, Oberlie F, Audetat A, Guillong M, Simon AC, Hanley JJ, Klemm LM (2012) Recent developments in element concentration and isotope ratio analysis of individual fluid inclusions by laser ablation single and multiple collector ICP-MS. *Ore Geol Rev* 44: 10–38
- Pillans B (2007) Pre-Quaternary landscape inheritance in Australia. *J Quat Sci* 22:439–447
- Pirajno F (2015) Intracontinental anorogenic alkaline magmatism and carbonatites, associated mineral systems and the mantle plume connection. *Gondwana Res* 27:1181–1216
- Pirajno F, González-Álvarez I (2013) The ironstone veins of the Gifford Creek ferrocyanite complex, Gascoyne Province: Geological Survey of Western Australia, Record 2013/12, pp 19
- Pirajno F, González-Álvarez I, Chen W, Kyser KT, Simonetti A, Leduc E, leGras M (2014) The Gifford Creek Ferrocyanite Complex, Gascoyne Province, Western Australia: associated fenitic alteration and a putative link with the ~1075 Ma Warakurna LIP. *Lithos* 202–203:100–119
- Pisarevsky SA, Wingate MTD, Li Z-X, Wang X-C, Tohver E, Kirkland CL (2014) Age and paleomagnetism of the 1210Ma Gnowangerup–Fraser dyke swarm, Western Australia, and implications for late Mesoproterozoic paleogeography. *Precambrian Res* 246:1–15
- Richter DK, Görge P, Götze T (2008) Monazite cathodoluminescence - a new tool for heavy mineral analysis of siliciclastic rocks. *Sediment Geol* 209:36–41
- Roncal-Herrero T, Rodríguez-Blanco JD, Oelkers EH, Benning LG (2011) The direct precipitation of rhabdophane (REEPO₄·nH₂O) nano-rods from acidic aqueous solutions at 5–100°C. *J Nanopart Res* 13:4049–4062
- Shannon RD (1976) Revised effective ionic radii and systematic studies of interatomic distances in halides and chalcogenides. *Acta Crystallographica Section A* 32:752–767
- Sheppard S, Occhipinti SA, Nelson DR (2005) Intracontinental reworking in the Capricorn Orogen, Western Australia: the 1680–1620 Ma Mangaroon Orogeny. *Aust J Earth Sci* 52:443–460
- Sheppard S, Rasmussen B, Muhling JR, Farrell TR, Fletcher IR (2007) Grenvillian-aged orogenesis in the Palaeoproterozoic Gascoyne Complex, Western Australia: 1030–950 Ma reworking of the Proterozoic Capricorn Orogen. *J Metamorph Geol* 25:477–494
- Sheppard S, Bodorkos SP, Johnson SP, Wingate MTD, Kirkland CL (2010) The Paleoproterozoic Capricorn Orogeny: intracontinental reworking not continent-continent collision. Geological Survey of Western Australia, Report 108, pp 33
- Slezak P, Spandler C (2019) Carbonatites as recorders of mantle-derived magmatism and subsequent tectonic events: an example of the Gifford Creek Carbonatite Complex, Western Australia. *Lithos* 328–329:212–227
- Slezak P, Spandler C (2020) Petrogenesis of the Gifford Creek Carbonatite Complex, Western Australia. *Contrib Mineral Petrol* 175(3):28
- Slezak P, Spandler C, Blake K (2018) Ghosts of apatite past: using hyperspectral cathodoluminescence and micro-geochemical data to reveal multi-generational apatite in the Gifford Creek Carbonatite Complex, Australia. *Can Mineral* 56:773–797
- Smith MP, Henderson P, Campbell LS (2000) Fractionation of the REE during hydrothermal processes: constraints from the Bayan Obo Fe-REE-Nb deposit, Inner Mongolia, China. *Geochim Cosmochim Acta* 64:3141–3160
- Smithies RH, Kirkland CL, Korhonen FJ, Aitken ARA, Howard HM, Maier WD, Wingate MTD, Quentin de Gromard R, Gessner K (2015) The Mesoproterozoic thermal evolution of the Musgrave Province in central Australia - plume vs. the geological record. *Gondwana Res* 27:1419–1429
- Spandler C, Pettke T, Rubatto D (2011) Internal and external fluid sources for eclogite-facies veins in the Monviso meta-ophiolite, Western Alps: implications for fluid flow in subduction zones. *J Petrol* 52:1207–1236
- Stark JC, Wang X-C, Li Z-X, Denysyn S, Rasmussen B, Zi J-W (2018) 1.39 Ga mafic dyke swarm in the southwestern Yilgarn Craton marks Nuna to Rodinia transition in the West Australian Craton. *Precambrian Res* 316:291–304
- Torpy A, Wilson NC (2008) OpticalFit software by CSIRO Australia
- Treiman AH (1989) Carbonatite magma: properties and processes. In: Bell K (ed) Carbonatites: genesis and evolution. Unwin Hyman, London, pp 89–104
- Van Achtenbergh E, Ryan CC, Jackson SE, Griffin WL (2001) Data reduction software for LA-ICP-MS. In: Sylvester PJ (ed) Laser-Ablation-ICP-MS in the earth sciences: principles and applications. Mineral Association of Canada, pp 239–243
- Van Emdem B, Thöni M, Graham J, Lincoln FJ (1997) The incorporation of actinides in monazite and xenotime from placer deposits in Western Australia. *Can Mineral* 35:95–104
- Vaughan APM, Scarrow JH (2003) K-rich mantle metasomatism control of localization and initiation of lithospheric strike-slip faulting. *Terra Nova* 15:163–169
- Verplanck PL, Mariano AN, Mariano A (2016) Rare earth element ore geology of carbonatites. In: Verplanck PL, Hitzman MW (eds) Rare earths and critical elements in ore deposits, vol 18. Society of Economic Geologists. Littleton, Colorado, pp 5–32
- Wade BP, Barovich KM, Hand M, Scrimgeour IR, Close DF (2006) Evidence of early Mesoproterozoic arc magmatism in the Musgrave Block, central Australia: implications for Proterozoic crustal growth and tectonic reconstructions of Australia. *J Geol* 114:43–63
- Wall F (2014) Rare earth elements. In: Gunn AG (ed) Critical metals handbook. Wiley, pp 312–339
- Wall F, Zaitsev AN (2004) Rare earth metals in Kola carbonatites. In: Wall F, Zaitsev AN (eds) Phoscorites and carbonatites from mantle to mine: the key example of the Kola Alkaline Province. The Mineralogical Society of Great Britain & Ireland, Cambridge, pp 341–373
- Walters A, Lusty P, Hill A (2011) Rare earth elements British Geological Survey mineral profiles. United Kingdom, pp 54
- Woolley AR, Kempe DRC (1989) Carbonatites: nomenclature, average chemical compositions, and element distribution. In: Bell K (ed) Carbonatites genesis and evolution. Unwin Hyman Ltd, London, pp 1–14
- Zaitsev AN, Frances W, Le Bas MJ (1998) REE-Sr-Ba minerals from the Khibina carbonatites, Kola Peninsula, Russia: their mineralogy, paragenesis and evolution. *Mineral Mag* 62:225–250
- Zi JW, Gregory C, Rasmussen B, Sheppard S, Muhling JR (2017) Using monazite geochronology to test the plume model for carbonatites: the example of Gifford Creek Carbonatite Complex, Australia. *Chem Geol* 463:50–60

Publisher's note Springer Nature remains neutral with regard to jurisdictional claims in published maps and institutional affiliations.